POLITECNICO DI MILANO

Facoltà di Ingegneria Industriale e dell' Informazione

Corso di Laurea Magistrale in Ingegneria Fisica

POLITECNICO
MILANO 1863

Resonant Inelastic X-ray Scattering of Iridium Fluorides

Relatore: Prof. Giacomo Claudio GHIRINGHELLI
Correlatore: Dott. Marco MORETTI

Tesi di Laurea di:
Roberto FUMAGALLI
Matr. 823760

Anno Accademico 2015 - 2016

to Alessandro, Matilde and Matteo

"It doesn't matter how beautiful your theory is,
it doesn't matter how smart you are.
If it doesn't agree with experiment, it's wrong."

Richard Feynman

Abstract

In this work, we will study the electronic properties of Ir fluorides by means of Resonant Inelastic X-ray Scattering (RIXS). The measurements were performed at ID20 beamline at the European Synchrotron Radiation Facility (ESRF), Grenoble. $5d$ transition metal oxides, iridates in particular, have recently been intensively explored as they display new fascinating phenomena, arising from the strong spin-orbit coupling to which they are subjected. The interest in iridium compounds is increased mostly following the theoretical prediction of high-temperature superconductivity [1], where the authors proposed this behaviour due to the similarity between the electronic structure of iridates and cuprates. The most known and well studied compound is Sr_2IrO_4 [2, 3, 4], a $J_{\mathrm{eff}} = \frac{1}{2}$ Mott insulator.

On the basis of electronic structure calculations, Birol *et al.* suggested that Rb_2IrF_6 may be characterised by a SU(2) symmetric ground state and therefore be a good candidate to host high-temperature superconductivity [5]. These materials have not been extensively characterized yet, and the main goal of this work is to examine their electronic structure. We therefore carried out extensive RIXS measurements in Rb_2IrF_6 and other Ir fluorides and developed a simple single-ion model for the interpretation of the data. Our results show that the effective trigonal/tetragonal crystal feld splitting of the $5d$-t_{2g} states is large. Contrarily to what the above-mentioned theoretical calculations predicted, we conclude that the ground state wavefunction in Ir fluorides is not close to the SU(2) symmetric case relevant for high-temperature superconductivity in iridates.

Sommario

L'obiettivo di questo lavoro è studiare la struttura elettronica e le relative proprietà degli iridati, in particolare fluoruri, utilizzando la tecnica spettroscopica RIXS (Resonant Inelastic X-ray Scattering). Questa tecnica spettroscopica viene usata per caratterizzare determinate proprietà dei materiali investigando le eccitazioni elementari. In particolare questa tecnica è utilizzata per studiare le proprietà elettroniche e magnetiche di sistemi correlati, come cuprati e iridati. Gli esperimenti sono stati effettuati presso la beamline ID20 del sincrotrone europeo (European Synchrotron Radiation Facility, ESRF) situato in Grenoble, Francia. I metalli di transizione $5d$, nello specifico i composti dell'iridio (iridati), hanno recentemente suscitato un notevole interesse data la scoperta di nuove proprietà fisiche, causate principalmente dal forte accoppiamento di spin-orbita che caratterizza questi sistemi. In particolare, lo studio di questi composti è cresciuto specialmente con la predizione teorica di un possibile comportamento superconduttivo ad alta temperatura critica, data la similitudine con la struttura elettronica, cristallina e magnetica dei cuprati. Il composto dell'iridio maggiormente studiato e caratterizzato è lo $\mathrm{Sr_2IrO_4}$, prototipo del $J_{\text{eff}} = \frac{1}{2}$ isolante di Mott.

Sulla base di calcoli della struttura elettronica, Birol *et al.* hanno recentemente mostrato che il composto $\mathrm{Rb_2IrF_6}$, data la simmetria del ground state (SU(2)), potrebbe essere un buon candidato nel mostrare un comportamento superconduttivo ad alta temperatura critica. Questo materiale, così come altri fluoruri dell'iridio, non è stato ancora completamente studiato e caratterizzato. L'obiettivo principale di questo lavoro è quello di studiarne la struttura elettronica. Per questo motivo abbiamo effettuato una serie di misure RIXS sul Rb_2IrF_6 e altri fluoruri dell'iridio, sviluppando inoltre un semplice modello a singolo ione per l'interpretazione dei dati. I risultati ottenuti mostrano un evidente splitting degli stati $5d$-t_{2g} causato dalla presenza di un campo cristallino tetragonale o trigonale. Contrariamente a quanto predetto dallo studio teorico della struttura elettronica del Rb_2IrF_6, possiamo concludere che i fluoruri dell'iridio non sono caratterizzati dall'avere simmetria SU(2), caso rilevante per la superconduttività ad alta temperatura negli iridati.

Contents

Abstract **ix**

Sommario **xi**

List of Figures **xiii**

List of Tables **xvii**

1 Introduction **1**

2 Physics of iridium compounds **5**

2.1 Strongly correlated electron systems 5

2.2 Iridates 7

2.2.1 Crystal field and d-levels splitting 8

2.2.2 Effect of spin-orbit coupling: the $J_{\text{eff}} = 1/2$ 9

2.2.3 Effect of non-cubic crystal field 13

3 Resonant Inelastic X-ray Scattering **17**

3.1 Introduction 17

3.2 The scattering process 20

3.3 RIXS cross-section 22

4 Experimental setup **27**

4.1 Synchrotron light source 27
4.1.1 Synchrotron radiation at the ESRF 28
4.2 ID20 beamline at the ESRF 29
4.2.1 General optical layout 30
4.2.2 The high-resolution IXS spectrometer 31

5 Iridium fluorides 37
5.1 Motivation for this work 37
5.2 Expermental details 39
5.3 Single-ion model Hamiltonian 45
5.4 Single-ion RIXS cross-section (trigonal case) 50
5.5 Results and discussion 52
5.6 Conclusions 58

A RIXS atomic scattering tensors 61
A.1 Trigonal case 61
A.2 Tetragonal case 63

Bibliography 67

Acknowledgments 73

List of Figures

1.1 Schematic phase diagram of a generic correlated system as a function of the electron-electron Coulomb repulsion U and the spin-orbit coupling ζ in unit of the hopping amplitude t. . . . 2
1.2 Crystal structure of Sr_2IrO_4 and La_2CuO_4. 3
1.3 Dispersion relation of La_2CuO_4 at T = 10 K and of Sr_2IrO_4 at T = 15 K. 3

2.1 The density of states (DOS) of electrons in a dynamical mean-field solution of the Hubbard model. 6
2.2 Octahedral geometry of Ir ion and splitting of $5d$ levels by octahedral crystal field and SOC. 8
2.3 Schematic band diagrams of $5d^5$ iridates levels. 10
2.4 Optical conductivity measurements on Sr_2IrO_4 at room temperature and oxygen $1s$ polarization dependent XAS spectra at 80 K. 11
2.5 Theoretical Fermi surfaces and band dispersion in LDA calculations on Sr_2IrO_4. 12
2.6 Resonant enhancement of the magnetic reflection across the Ir $L_{2,3}$-edge at 10 K and calculation of X-rays scattering matrix elements of a Sr_2IrO_4 single crystal. 13
2.7 Effect of the non-cubic crystal field on the IrO_6 octahedra. . . 14

2.8 Sr_3CuIrO_6 RIXS measurements. 14

3.1 Different elementary excitations in condensed matter physics accesible by RIXS. 18
3.2 Cu L_3 absorption spectrum, decomposition of the La_2CuO_4 spectrum at $q_{//} = 1.85$ and single magnon dispersion obtained using RIXS and Inelastic Neutron Scattering. 19
3.3 Scheme of direct RIXS process. 21
3.4 Scheme of the kinematic and conservation laws involved in RIXS process 21

4.1 Schematic representation of a typical third-generation facility, in this case the ESRF. 28
4.2 Design of the ESRF storage ring. 29
4.3 Optical layout of the ID20 beamline. 30
4.4 KB chamber and high-resolution IXS spectrometer. 32
4.5 Rowland circle geometry and the diced analyser in detail. . . . 33
4.6 Measured elastic peak on a polymer sample in order to calculate the instrumental energy resolution. 34

5.1 Crystal structure of compounds with chemical formulae A_2IrF_6. 38
5.2 Spectral function and DOS of Rb_2IrF_6 as given by DFT calculations 38
5.3 Incident energy dependence of Ir L_3-edge RIXS spectra measured on Rb_2IrF_6 powder sample at 300 K. 40
5.4 Ir L_3-edge XAS spectrum of Rb_2IrF_6. 40
5.5 RIXS spectrum of Rb_2IrF_6 powder obtained with E_i=11.219 keV at 300 K. 42
5.6 RIXS spectra of various iridium fluorides at 10 and 300 K. . . 43
5.7 Temperature dependence of d-d excitations in Na_2IrF_6 and zoom on the low energy ($\sim$ 0.43 eV) feature at 300 K. 44
5.8 Dependence of the wavefunction, eigenvalues and orbital occupancies on the effective trigonal crystal field splitting. 49

5.9 Simulated RIXS spectra of Rb_2IrF_6 in the case of $\Delta_{tri} > 0$ and $\Delta_{tri} < 0$. 53
5.10 Effective trigonal/tetragonal crystal field splitting and spin-orbit coupling of the various compounds at 10 and 300 K . . . 55
5.11 Effective tetragonal crystal field splitting of Na_2IrF_6 in the temperature range between 10 and 310 K. 56
5.12 RIXS spectrum of Na_2IrF_6 at 235 K. 57
5.13 Plot of relative amplitudes of the two peaks A and B in Na_2IrF_6. 58

A.1 ID20 beamline staff. 74

List of Tables

5.1 Results of the fitting to the spectra of Fig. 5.6. 43

5.2 Effective trigonal/tetragonal crystal field splitting and spin-orbit coupling of the various compounds at 10 and 300 K. . . 54

5.3 Effective tetragonal crystal field splitting and spin-orbit coupling of Na_2IrF_6 in the temperature range between 10 and 310 K. 56

5.4 Relative amplitude of peak A and B in Na_2IrF_6. 58

Chapter 1

Introduction

In this work, we will study the electronic properties of Ir fluorides by means of Resonant Inelastic X-ray Scattering (RIXS). The great interest in Ir compounds is due to the exotic physical properties they display as a result of a subtle balance between electron correlation effects and spin-orbit coupling, as shown in Fig. 1.1. As an example, we mention the spin-orbit assisted metal-to-insulator transitions in Sr_2IrO_4 and other oxides [3] and the bond-directional nature of magnetic interactions in Na_2IrO_3 and Li_2IrO_3 [6].

Ir compounds, or iridates, are also intensively studied because of their resemblance to cuprates, well-known materials displaying unconventional superconductivity at relatively high temperature [8]. Many properties of cuprates can be found in iridates, including their crystal [9, 10], magnetic [4, 11, 12] and electronic [3, 13] structure and dynamics [14, 15, 16, 17, 18]. Crystal structures and magnetic dispersions of Sr_2IrO_4 and La_2CuO_4 are shown in Fig. 1.2 and 1.3, respectively. In addition, it was theoretically predicted that Sr_2IrO_4 and other iridium oxides may display high-temperature superconductivity when electron doped [1]. Indeed, the similarities with cuprates also extend to the metallic regime: Fermi arcs and a *d*-wave gap were observed in the high and low temperature phases, respectively, of surface K-doped Sr_2IrO_4 [19, 20]. Despite intense effort has been devoted to the study of doped Sr_2IrO_4 [21, 22], however, a direct experimental proof of

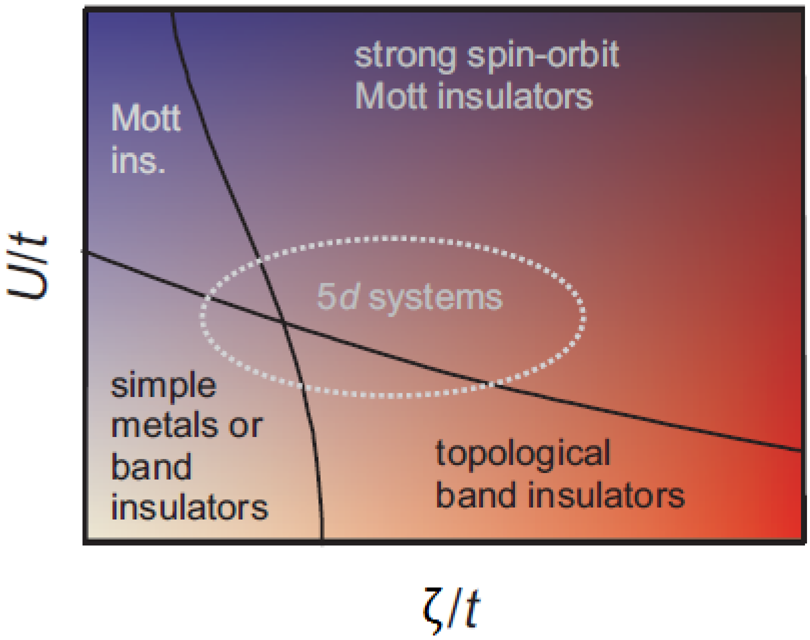

Figure 1.1: Schematic phase diagram of a generic correlated system as a function of the electron-electron Coulomb repulsion U and the spin-orbit coupling ζ in unit of the hopping amplitude t. At the center of the phase diagram, where electronic correlations and spin-orbit coupling are equally relevant, one can find $5d$ electron systems, such as iridates. Figure taken from Ref. [7].

unconventional superconductivity in iridates is still missing.

Recently, the attention was drawn on a different class of iridates, Ir fluorides. On the basis of electronic structure calculations, Birol *et al.* suggested that Rb_2IrF_6 may be characterised by a SU(2) symmetric ground state and therefore be a good candidate to host high-temperature superconductivity [5]. These materials have not been extensively characterized yet, and the main goal of this work is to examine their electronic structure. We therefore carried out extensive RIXS measurements in Rb_2IrF_6 and other Ir fluorides and developed a simple single-ion model for the interpretation of the data.

The manuscript is organised as follows: in Chapter 2 we introduce the reader to the physics of Ir compounds, including milestone experiments and the so-called $J_{\text{eff}} = 1/2$ model that was introduced to explain the insulating properties of the benchmark compound Sr_2IrO_4. In Chapter 3, RIXS is pre-

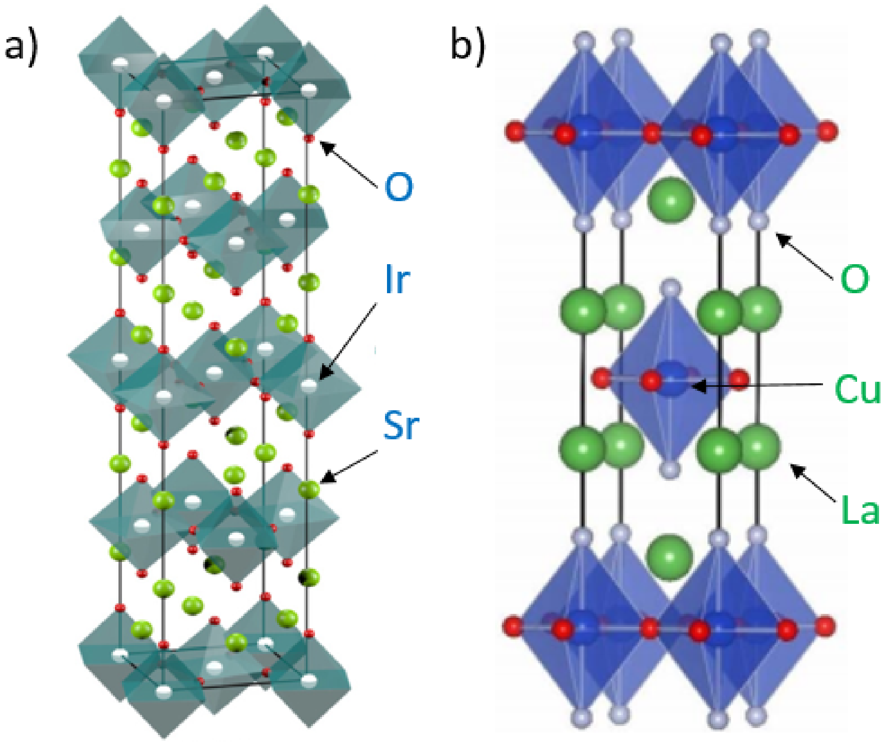

Figure 1.2: Crystal structure of Sr_2IrO_4 (a) and La_2CuO_4 (b). Figures taken from Ref. [23] and [24].

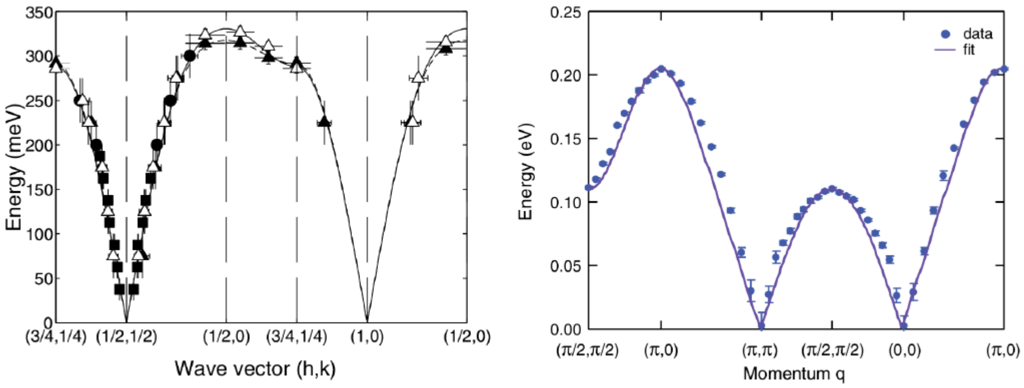

Figure 1.3: Dispersion relation of La_2CuO_4 (right) at T = 10 K and of Sr_2IrO_4 (left) at T = 15 K. Figure taken from Ref. [17] and [14].

sented together with a minimal theoretical background for the interpretation of the spectra. Chapter 4 overviews the experimental set-up we used to perform RIXS measurements at the ID20 beamline of the ESRF. Chapter 5 is the central chapter of the thesis, it contains the experimental results and their interpretation on the basis of the single-ion model. Conclusions are drawn at the end of Chapter 5.

Chapter 2

Physics of iridium compounds

In this chapter we will introduce the main features of correlated electrons systems such as $5d$ transition metal oxides (TMOs) and highlight similarities and differences with respect to the much more studied $3d$ counterpart. In particular we will focus on Ir-based compounds and the role of spin-orbit coupling in driving fascinating properties, such as a Mott insulating ground state, often termed $J_{\text{eff}} = 1/2$.

2.1 Strongly correlated electron systems

Strongly correlated electron systems are a wide class of compounds in which electron–electron interaction is large and drastically affects the physical properties. These systems can hardly be described by one–electron theories, where one electron interacts with an average potential generated by the effective motion of all other electrons. In correlated systems, instead, this approach usually does not work and electron–electron interaction can not be treated as a moderate perturbation, but should rather be considered predominant. Strongly correlated electron systems have partially filled outermost d or f electronic shells with narrow energy bands. In the non-interacting picture, this would lead to a metallic behaviour. However, strong electron–electron interaction prevents the electrons from moving freely in the solid and often

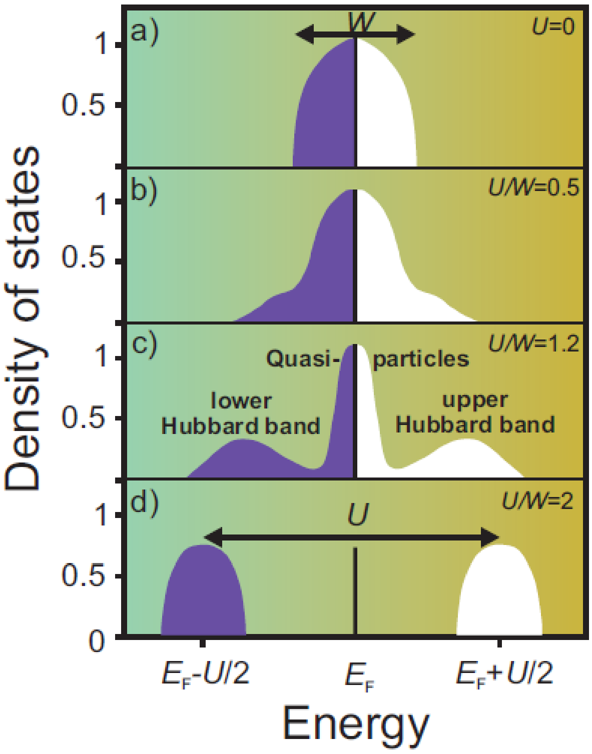

Figure 2.1: The density of states (DOS) of electrons in a dynamical mean-field solution of the Hubbard model where U is the Coulomb interaction energy and W the bandwidth of non-interacting electrons which is proportional to the hopping integral. (a) For $U = 0$ it is the metallic case, in which the Fermi level is located in the middle of the band. In the weakly correlated regime the ratio U/W is small and electrons can be classified as quasiparticle whose DOS resembles the one of free electrons. If $U/W > 1$ the correlation increases and the spectrum (c) shows three peaks that are typical in correlated metals. Finally (d), in the strong correlated regime ($U/W \gg 1$) a Mott-Hubbard transition to an insulating state takes place. Figure taken from Ref. [25].

produce an insulating ground state.

One of the most used and simple theoretical models that properly describes the electronic and magnetic properties of $3d$ strongly correlated electrons systems is the single-band Hubbard model [26]. This is an extension of the tight-binding model, in which electron–electron correlation is introduced by adding an energy cost term when two electrons occupy the same lattice site:

this is usually referred to as the on-site Coulomb repulsion, U. The Hubbard Hamiltonian reads

$$\mathcal{H} = \sum_{i,j} \sum_{\sigma} t_{ij} (\mathbf{c}^{\dagger}_{i\sigma} \mathbf{c}_{j\sigma} + \mathbf{c}^{\dagger}_{j\sigma} \mathbf{c}_{i\sigma}) + U \sum_{i} \mathbf{n}_{i\uparrow} \mathbf{n}_{i\downarrow} \tag{2.1}$$

where t_{ij} is the hopping integral, $\mathbf{c}^{\dagger}_{i\sigma}(\mathbf{c}_{i\sigma})$ are the creation (annihilation) operators of electrons with spin σ and $\mathbf{n}_{i\sigma} = \mathbf{c}^{\dagger}_{i\sigma}\mathbf{c}_{i\sigma}$ is the number operator. The physics of the system is dictated by the relative strength of electron localisation (U) and delocalisation (t). Specifically, the system is metallic if $U/t \rightarrow 0$ and it is so-called Mott insulator in the opposite limit ($U/t \rightarrow \infty$) because double occupancy of a single site is energetically unfavourable. We therefore expect a metal-to-insulator transition between these two regimes, which is usually called "Mott-Hubbard" transition. The evolution of the density of states of a model material as a function of the U/t (or U/W, where W is the bandwidth) is shown in Fig. 2.1. For U=0 the Fermi level lies in the middle of the valence band. Larger values of U affect the shape of the density of states by moving states away from the Fermi level. In the large U limit, two bands are formed, one entirely filled below the Fermi energy and one entirely empty above; these two bands are usually called the lower Hubbard (LHB) and the higher Hubbard bands (UHB), respectively. Their energy separation, the band gap, is somehow proportional to U.

2.2 Iridates

It has been proposed that Sr_2IrO_4, the prototypical iridium oxide, is a spin-orbit induced Mott insulator [3]. As we already mentioned, the Mott insulating state arise from the electron localisation in the strong U/t limit. However, when moving from $3d$ to $5d$ electron systems, the radial extension of electronic orbitals increase with two main consequences: U decreases because the electron cloud is spread over a larger portion of space and t increases because of a larger overlap between adjacent orbitals. Both these effects acts against the realisation of a Mott insulating state, contrarily to experimental findings: indeed, Sr_2IrO_4 is an insulator, with a band gap of approximately 0.2 eV [27]. It was therefore proposed that the combined action of spin-orbit coupling and a large crystal field facilitates the stabilisation of an insulating state, as explained in the following.

2.2.1 Crystal field and d-levels splitting

The electronic configuration of Ir ($Z = 77$) is $[Xe]4f^{14}5d^7 6s^2$. Because the $4f$ electronic shell is full, only the $5d$ and $6s$ shells actively participate in the chemical bonding, while the remaining electrons can be considered as core–electrons. In a pure ionic picture each Ir donates four electrons to the neighbouring O, leading to a Ir^{4+} ($5d^5$) and O^{2-} ($2p^6$) electronic configurations. The Ir^{4+} ion in Sr_2IrO_4 is trapped in a cage of O^{2-} ions with sixfold coordination [10] (Fig. 2.2(a)).

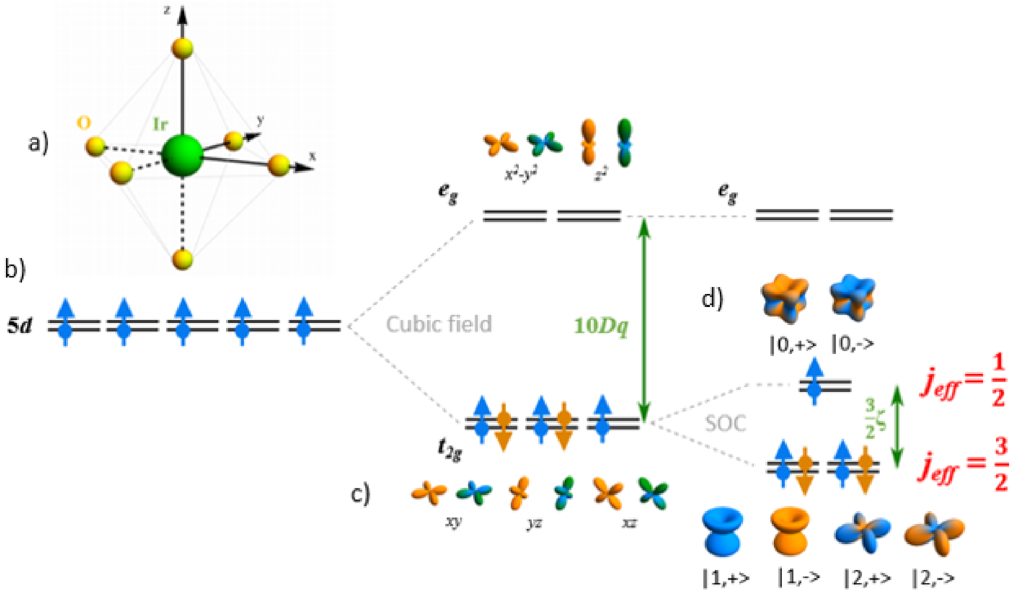

Figure 2.2: a) Illustration of the Ir ion in an octahedral environment of O ligands. b) $5d$ levels splitted by the crystal field $10Dq$ and the spin-orbit coupling ζ. Visualization of the t_{2g} and e_g wave functions (c) and the composition of the $J_{\text{eff}} = 1/2,\, 3/2$ orbitals (d).

In the crystal field model, the O^{2-} ions are considered as point charges that break the spherical symmetry of the potential and lead to a splitting of the $5d$ states, as shown in Fig. 2.2(c). The eigenstates of the Hamiltonian with octahedral symmetry are linear combinations of spherical harmonics and are usually classified in two classes, the triply degenerate t_{2g} (d_{xy}, d_{yz} and d_{xz}) states and the doubly degenerate e_g ($d_{x^2-y^2}$ and $d_{3z^2-r^2}$) states [28]. Their energy separation is called crystal field splitting and is usually indicated by $10Dq$. In particular, the e_g orbitals lie at higher energies than the t_{2g} states (if $10Dq > 0$) because their lobes are directed towards the O^{2-} ions, while the t_{2g} orbitals point in between, making their interaction with the O^{2-} ions different. In Ir compounds (octahedral O_h point group symmetry) the crystal field splitting is large ($10Dq \sim 3$ eV [29, 30, 31, 32]): the electrons partially fill the t_{2g} levels forming a low-spin state ($S = 1/2$), while leaving the e_g states empty; as a consequence, the e_g orbitals are usually neglected in the description of the electronic properties of iridates.

2.2.2 Effect of spin-orbit coupling: the $J_{\text{eff}} = 1/2$

Spin-orbit coupling (SOC) is a relativistic effect that links the spin and orbital angular momenta of an electron. The SOC Hamiltonian can be written as

$$\mathcal{H}^{SOC} = \zeta \mathbf{L} \cdot \mathbf{S} \tag{2.2}$$

where $\mathbf{L}$ and $\mathbf{S}$ are the total orbital and spin momentum operators and ζ is the strength of the interaction. For $3d$ TM ions, the SOC is considered as a small perturbation because substantially smaller ($\zeta_{3d} \sim$ 20-40 meV [33]) than both crystal field ($10Dq$) and the on-site Coulomb interaction (U). In the case of heavier ions such as $4d$ and $5d$ TM, spin-orbit coupling interaction increases and can no longer be treated as a small perturbation ($\zeta_{5d} \sim$ 200-500 meV [34]). The effect of the SOC on the t_{2g} subspace is to remove the three-fold degeneracy by splitting these states in the $J_{\text{eff}} = 3/2$ quartet at lower energy and the $J_{\text{eff}} = 1/2$ doublet at higher energy (Fig. 2.2(d)). With five electrons filling the $5d$-t_{2g} states, the $J_{\text{eff}} = 3/2$ quartet is fully occupied and the $J_{\text{eff}} = 1/2$ doublet is half filled. The ground state of iridates is therefore described by one hole occupying the $J_{\text{eff}} = 1/2$ ground state [3]. The splitting between the $J_{\text{eff}} = 1/2$ ground state and the $J_{\text{eff}} = 3/2$ state is $3\zeta/2$. Note that the $J_{\text{eff}} = 1/2$ and $J_{\text{eff}} = 3/2$ splitting of the $5d$-t_{2g} levels can be accounted for by considering the action of spin-orbit coupling on p-like states ($L = 1$) with an effective orbital angular momentum $L_{eff} = -L$ [35].

It is important to notice that this discussion is valid only if the e_g levels can be neglected, that is when $10Dq \gg \zeta$. In this case, the $J_{\text{eff}} = 1/2$ ground state is given by an even admixture of the three t_{2g} orbitals d_{xy}, d_{yz} and d_{xz} [3]:

$$|J_{\text{eff}} = 1/2, \pm\rangle = \frac{\pm |d_{xy}, \pm\rangle + |d_{yz}, \mp\rangle \pm i\, |d_{xz}, \mp\rangle}{\sqrt{3}} \tag{2.3}$$

where ± represents the spin polarization. The case in which the crystal field symmetry is lower than octahedral is presented in Chapter 5.

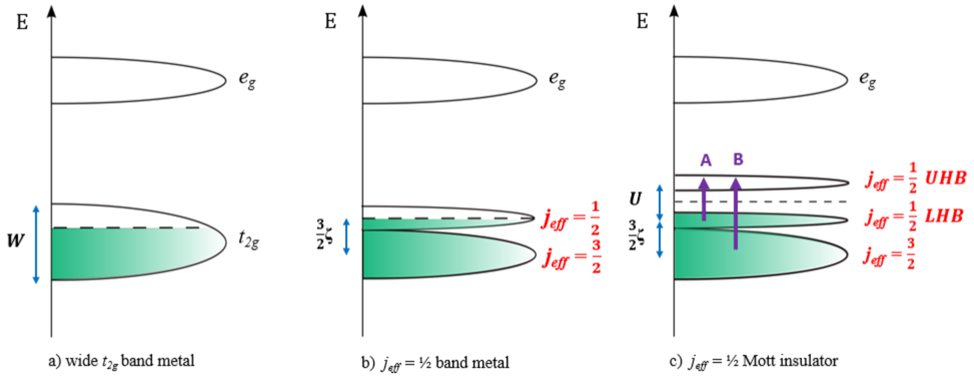
E
e_g
W
t_{2g}
a) wide t_{2g} band metal
E
e_g
$\frac{3}{2}\zeta$
$j_{eff} = \frac{1}{2}$
$j_{eff} = \frac{3}{2}$
b) j_{eff} = ½ band metal
E
e_g
A
B
U
$\frac{3}{2}\zeta$
$j_{eff} = \frac{1}{2}$ UHB
$j_{eff} = \frac{1}{2}$ LHB
$j_{eff} = \frac{3}{2}$
c) j_{eff} = ½ Mott insulator

Figure 2.3: Schematic band diagrams of $5d^5$ iridates levels: a) without SOC contribution $W \gg U$ and the system has a metallic behaviour; b) including SOC, the t_{2g} band is split into the $J_{\text{eff}} = 1/2$ doublet at higher energy and in the $J_{\text{eff}} = 3/2$ quartet. c) Adding a relatively small U a Mott gap appears driving the system to the insulating state. A and B represent possible optical transitions.

The electronic structure resulting from the combined action of crystal field splitting and spin-orbit interaction is a narrow half filled $J_{\text{eff}} = 1/2$ ground state (Fig. 2.3(b)). The corresponding bandwidth is extremely small and therefore even a moderate on-site Coulomb repulsion can lead to electron localisation and the opening of a gap between a filled $J_{\text{eff}} = 1/2$-derived lower Hubbard (LHB) and an empty $J_{\text{eff}} = 1/2$-derived higher Hubbard (UHB) bands (Fig. 2.3(c)). It was argued that the effect of crystal field only would not lead to a sufficiently narrow band (Fig. 2.3(a)); because the role of spin-orbit coupling is crucial in order to branch off the $J_{\text{eff}} = 1/2$-derived band, such a Mott insulating state is said to be spin-orbit induced. Several iridium compounds such as layered perovskites ($Sr_3Ir_2O_7$ [36], Sr_2IrO_4 [2], Ba_2IrO_4 [37]), pyrochlores (R_2IrO_7 [38]) and other crystal structure (Na_2/Li_2IrO_3 [39] and $CaIrO_3$ [40]) have been proposed as spin-orbit induced Mott insulators. This model for iridates has been proposed for the first time by B. J. Kim *et al.* [3] based on Angle Resolved Photoemission Spectroscopy (ARPES), X-ray Absorption Spectroscopy (XAS), optical conductivity measurements and first-principle band structure calculations for Sr_2IrO_4.

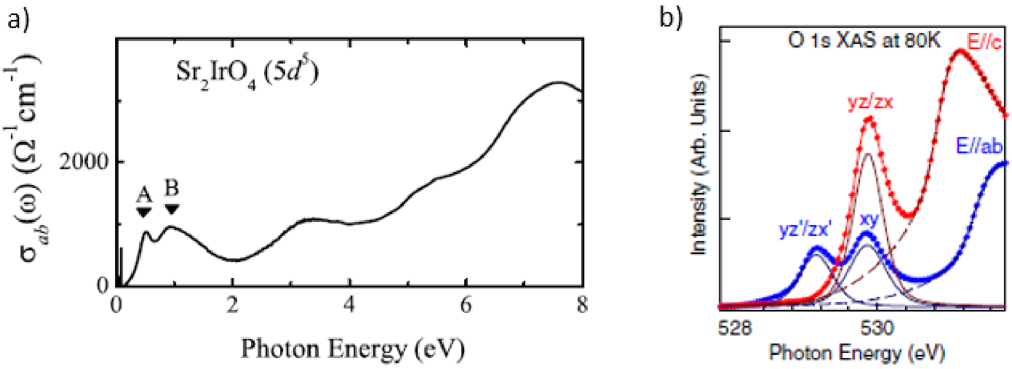

Figure 2.4: a) Optical conductivity measurements on Sr_2IrO_4 at room temperature. The A and B peaks correspond to the optical transitions illustrated in Fig. 2.3 which are attributable to the splitting of the t_{2g} levels. b) Oxygen 1s polarization dependent XAS spectra at 80 K (dottet lines) compared with the expected spectra (solid lines) considering an equal occupancy ratio of the xy, yz and xz orbitals. Figures taken from Ref. [29] and [3].

Fig. 2.4(a) shows an optical conductivity spectrum of Sr_2IrO_4. It display two features, A and B, at approximately 0.5 and 1 eV; according to the model described above, these features were interpreted as transitions between the $J_{\text{eff}} = 3/2$ and the LHB to the UHB (see Fig. 2.3(c)). Other peaks above 3 eV are associated to charge transfer transitions between the O $2p$ and the Ir $5d$ bands. The model also provides an interpretation for linear dichroic effects observed in XAS measurements at the O K-edge shown in Fig. 2.4(b). Absorption transitions at the O K-edge XAS arise from the hybridisation between the transition metal $5d$ states and the ligand $2p$ states and for this reason it can be used to investigate the $5d$ transition metal states. The two peaks in Fig. 2.4(b), in particular, are due to transitions occurring at the in-plane and out-of-plane oxygen sites and show distinct dichroism effect. The integrated spectral weight is related to the orbital occupation of the various orbitals; specifically, the spectral weight of the yz'/zx' and xy peaks is the same and half that of the yz/zx peak, which suggests an even admixture of the d_{xy}, d_{yz} and d_{zx} orbitals in the ground state, consistent with the $J_{\mathrm{eff}} = 1/2$ model. Finally, ARPES measurements shown in Fig. 2.5(e) show that the $J_{\mathrm{eff}} = 1/2$ LHB bandwidth is very narrow, approximately 0.5 eV (Fig. 2.5(c)), *e. g.* too small to be associated to the totality of the $5d$–t_{2g} states, as confirmed by DFT-LDA calculations in the absence of SOC (Fig. 2.5(a)). These, instead, nicely reproduce the experimental results only when SOC and on-site Coulomb interaction are included, LDA+SOC+U (Fig. 2.5(b)).

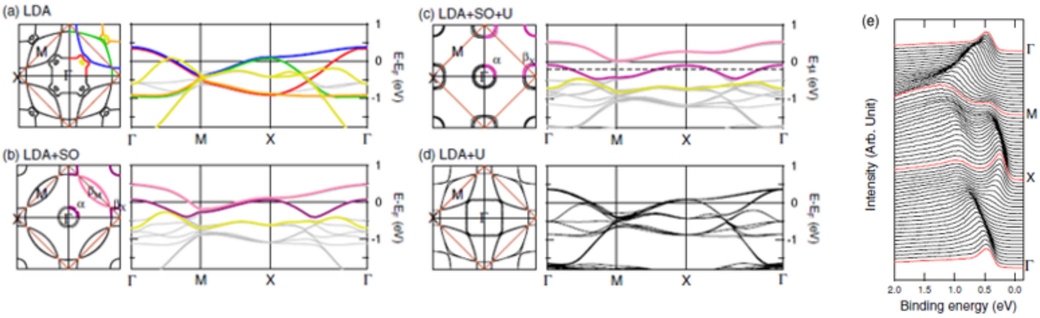

Figure 2.5: a) - d) Theoretical Fermi surfaces and band dispersion in LDA calculations on Sr_2IrO_4: the $J_{\mathrm{eff}} = 1/2$ is realized only taking into account SOC and a relative small U. e) ARPES data along high symmetry directions. Figures taken from Ref. [3].

More recently, a criterion has been proposed to identify the $J_{\mathrm{eff}} = 1/2$ ground state in novel Mott insulator iridates using X-rays Resonant Magnetic

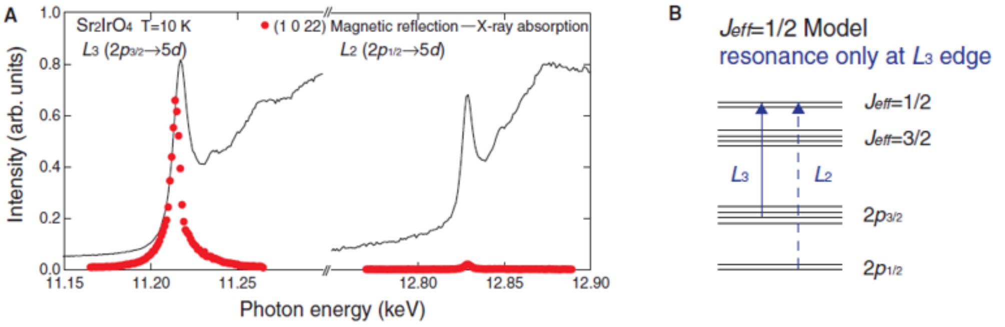

Figure 2.6: Resonant enhancement of the magnetic reflection across the Ir $L_{2,3}$-edge at 10 K (A) and calculation of X-rays scattering matrix elements of a Sr_2IrO_4 single crystal (B). Red lines represent the intensity of the magnetic peak, while the black ones are XAS spectra at the Ir $L_{2,3}$-edges. Figures taken from Ref. [4].

Scattering (XRMS): for a $J_{\text{eff}} = 1/2$ iridate in perfect octahedral symmetry, magnetic reflections are enhanced at the Ir L_3-edge and are vanishing at the Ir L_2-edge [4, 41] as shown in Fig. 2.6(a). This behaviour is readily explained by calculating the XRMS cross-section at a single ion level for magnetic moment oriented along the z axis. However, it was shown that this is no longer the case when the magnetic moment points in an arbitrary direction, in which case the XRMS L_2-edge is vanishing irrespective of the symmetry of the crystal field [30].

2.2.3 Effect of non-cubic crystal field

So far we only considered the case in which the symmetry of the crystal field is perfectly cubic. In actual materials, however, the symmetry is never exactly cubic and the symmetry of the crystal field is usually lower. In iridates, the most typical deviations are elongation/compression of the IrO_6 octahedra along the [0 0 1] (tetragonal case) or the [1 1 1] (trigonal case) directions, as it is illustrated in Fig. 2.7.

The consequence of the non-cubic symmetry is a change in the electronic structure of the 5d states: as shown in Fig. 2.7, the $J_{\text{eff}} = 1/2$ and $J_{\text{eff}} = 3/2$ bands mix forming the generic $|0, \pm\rangle$, $|1, \pm\rangle$ and $|2, \pm\rangle$ states, with

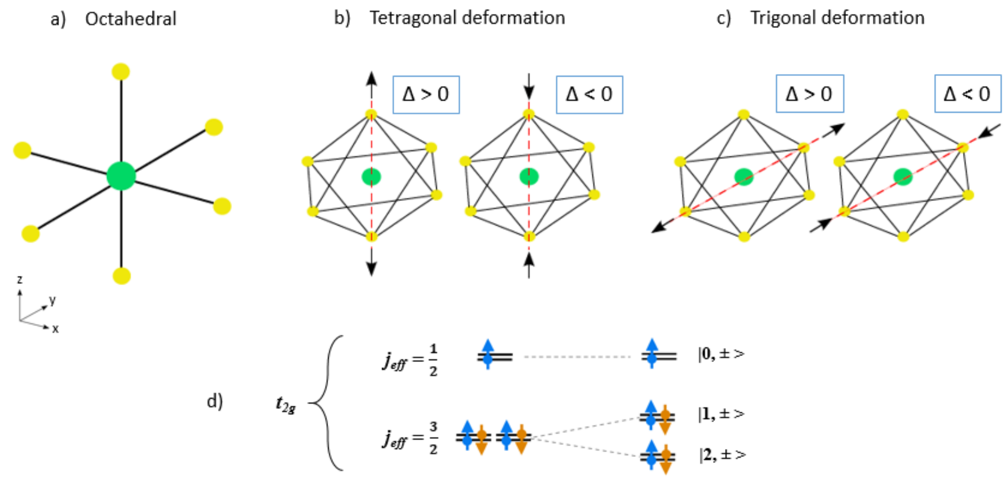
a) Octahedral
b) Tetragonal deformation
c) Trigonal deformation
Δ > 0
Δ < 0
Δ > 0
Δ < 0
z
y
x
d)
t_{2g}
$j_{eff} = \frac{1}{2}$
$j_{eff} = \frac{3}{2}$
|0, ± >
|1, ± >
|2, ± >

Figure 2.7: Effect of the non-cubic crystal field on the IrO_6 octahedra. a) No distortion, perfect cubic crystal field, b) tetragonal distortion due to an elongation ($\Delta > 0$) or compression ($\Delta < 0$) along the [0 0 1] direction and c) trigonal distortion along the [1 1 1] direction. In d) the evolution of the Ir t_{2g} levels is shown : the SOC coupling splits these states into a $J_{\text{eff}} = 1/2$ and $J_{\text{eff}} = 3/2$ bands and the tetragonal/trigonal component of the crystal field leads to a mixing of these orbitals removing the degeneracy of the $J_{\text{eff}} = 3/2$. The three new states $|0, \pm\rangle$, $|1, \pm\rangle$ and $|2, \pm\rangle$ are the so-called Kramers doublets.

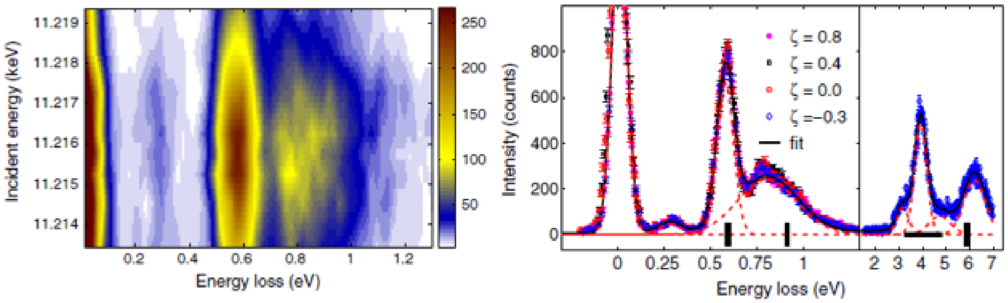

Figure 2.8: On the left the RIXS color map of Sr_3CuIrO_6 at Ir L_3-edge is shown. On the left side a RIXS spectrum measured at an incident energy of 11.216 keV is shown. The two peaks at ~ 0.6 and 0.8 eV correspond to intra-t_{2g} excitations. Figures taken from Ref. [42].

different admixture of d_{xy}, d_{yz} and d_{xz} states. The splitting of these states depends on the value of the SOC constant ζ and the non-cubic crystal field component Δ. Tetragonal [18, 31, 42] and trigonal [43, 44, 45] distortions of the octahedral crystal field had to be taken into account to explain Ir L_3-edge RIXS measurements in a number of compounds. As an example, we report in Fig. 2.8 RIXS measurements on Sr_3CuIrO_6. The double peak structure between 0.5 and 1 eV suggests a clear deviation from the $J_{\text{eff}} = 1/2$ ground state in the octahedral limit, as explained in Chapter 5.

Chapter 3

Resonant Inelastic X-ray Scattering

In this chapter we describe the Resonant Inelastic X-ray scattering (RIXS) technique. RIXS is an energy loss technique, which is used to characterize material properties by probing its elementary excitations [46, 47, 48, 49, 50, 51, 52, 53]. RIXS has been known for long [54], but it is only after the advent of third generation synchrotron radiation facilities and the development of dedicated instrumentation that it is extensively employed.

RIXS is suitable to investigate the electronic and magnetic structure of correlated electron systems such as iridates [49]. In the following we introduce the scattering process and the main characteristics of this technique together with a brief theoretical description of the RIXS cross-section.

3.1 Introduction

RIXS is a "photon *in* - photon *out*" synchrotron-based spectroscopy technique particularly suited to probe different types of excitations. In RIXS, an incoming monochromatic photon is scattered by the sample in an arbitrary direction and with a given energy, polarization state and momentum. The incident energy is chosen such that it coincides with one of the atomic transitions of the system under study, greatly enhancing the scattering cross-section.

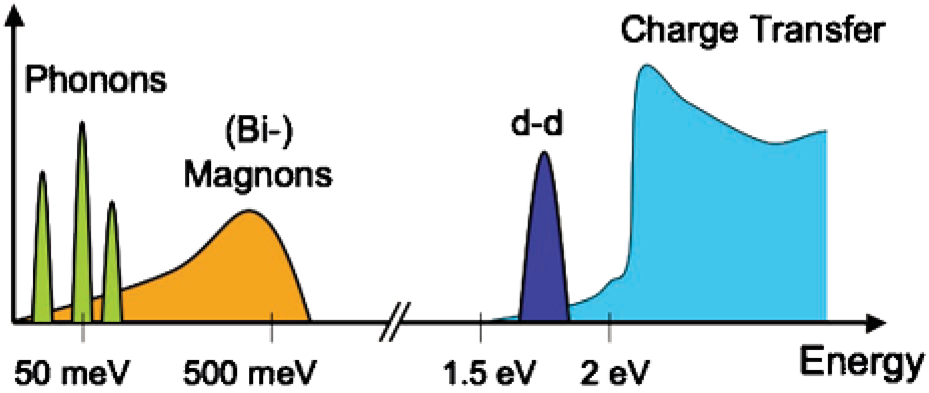

Figure 3.1: Different elementary excitations in condensed matter physics accesible by RIXS. Figure taken from Ref. [46].

A representative RIXS spectrum is sketched in Fig. 3.1 where the scattered photon intensity is reported as a function of the energy transferred to the sample during the process. The elementary excitations accessible by RIXS span in the range from phonons and magnons at the meV scale to *d*-*d* excitations and charge transfer at few eV. Analysing the inelastic features one can infer about the energy, momentum-dependence, symmetry and physical origin of the excitations occurred in the sample and ultimately about its ground state properties.

What makes RIXS an important research tool and a unique technique for the study of elementary excitations is:

- **element selectivity**: is it possible to excite selectively one specific element choosing the energy of the incident photon close to the corresponding absorbtion edge;
- **q-resolution**: in a typical RIXS experiment (particularly in the hard X-rays regime, where the wavelength of the incident X-rays beam is ~ 1 Å, *e. g.* comparable with the typical interatomic distances) elementary excitations can be mapped in reciprocal space. As we know, a photon carries momentum which is inversely proportional to its wavelength. For small energy losses, the momentum transferred in the scattering

process is defined by

$$\frac{4\pi\hbar}{\lambda}\sin\theta \tag{3.1}$$

where 2θ is the scattering angle and λ the wavelength of the incoming radiation.

- **neutrality**: during the scattering process there are not charges added or removed from the sample. Therefore the neutrality of the sample is preserved during RIXS measurements, unlike ARPES, therefore making the interpretation of results easier;
- **bulk sensitivity**: the large penetration depth is ensured by the use of X-ray photons. At the Ir L_3-edge of iridates, for example, it is in the order of several μm.

The renewed interest in this technique is due to the recent instrument developments that pushed the energy resolution of RIXS experiments down to the energy scale of valence electron excitations and the discovery that RIXS is sensitive to magnetic excitations [15, 55].

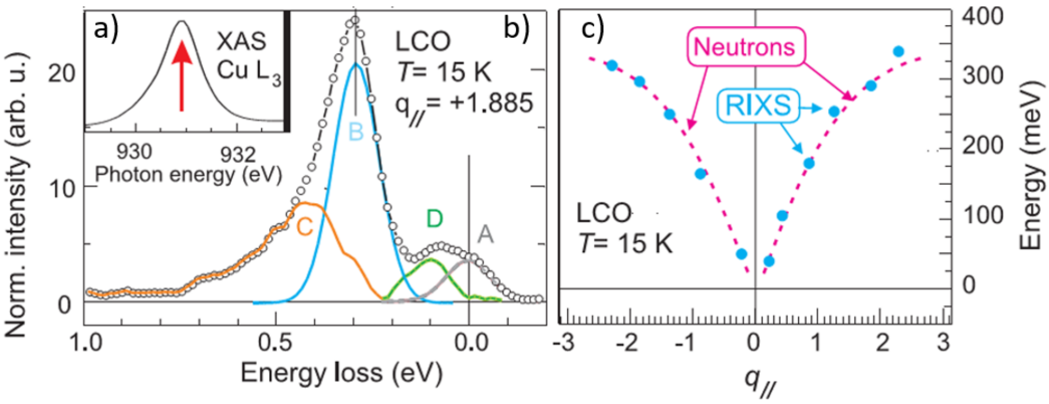

Figure 3.2: Panel a): Cu L_3 absorption spectrum, where the red arrow indicates excitation energy. Panel b): decomposition of the LCO (La_2CuO_4) spectrum at $q_{//} = 1.85$ where elastic peak (A), single magnon (B), multiple magnons (C) and optical phonons (D) are shown. Panel c) shows the single magnon dispersion obtained using RIXS (blu dotted line) and Inelastic Neutron Scattering (INS). Figures taken from Ref. [15].

The dispersion of magnons has traditionally been studied using Inelastic Neutron Scattering (INS), because neutrons are more suitable to probe magnetic excitations since they couple directly to the electron spin moment. Fig. 3.2(c) shows that the dispersions of magnetic excitations measured by INS and RIXS in undoped antiferromagnetic La_2CuO_4 coincide. This has been an important turning point as it opens the possibility to study magnetic excitations is samples where the neutrons fall short, *e. g.* in the case of very small volume samples and with samples containing strong neutron absorbers, like Ir.

3.2 The scattering process

As illustrated in Fig. 3.3, direct RIXS is a second order process that is usually described as a two-step process: by absorption of an X-ray of energy $\hbar\omega_i$, a core electron is promoted to an empty state in the valence band (above the Fermi level), thus creating a highly excited intermediate state, with $\sim$ fs typical lifetime. After this time, by virtue of the radiative recombination of the core hole with a valence electron, the system decays into a final state (not necessarily coinciding with the initial state) by emitting another X-ray photon with energy $\hbar\omega_o$. The difference in energy between the incident and emitted X-rays defines the final state energy of the system. Because of conservation of energy and momentum, the final state is characterised by an energy loss E and momentum transfer $\hbar\mathbf{q}$

$$\hbar\omega_i - \hbar\omega_o = E \tag{3.2}$$

$$\hbar\mathbf{k}_i - \hbar\mathbf{k}_o = \hbar\mathbf{q}. \tag{3.3}$$

These considerations are schematically reported in Fig. 3.4. There is also another conservation law regarding the polarization state of the photons ($\epsilon_{i,o}$), which derives from the conservation of the total angular momentum of the system. Unfortunately, however, polarisation of the scattered photon energy is not routinely performed in current RIXS measurements and information on the scattered photon polarisation is lost.

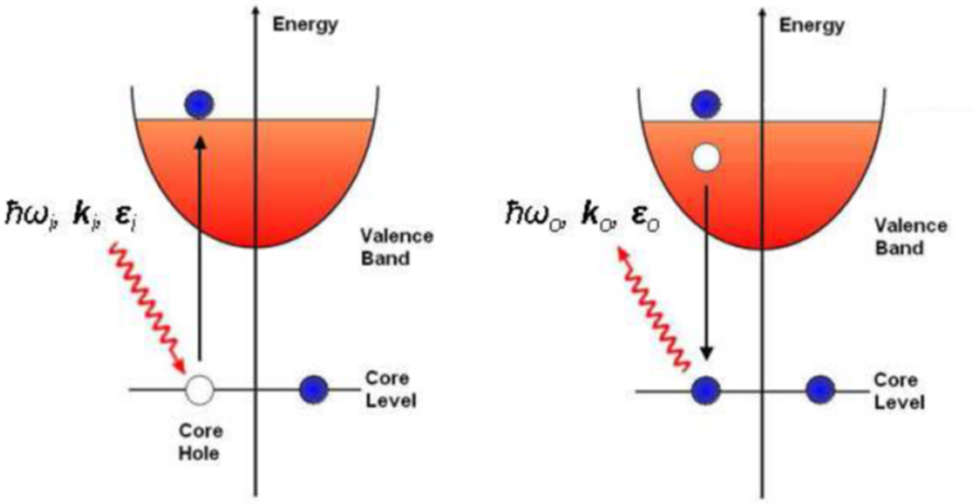
Energy
ħω_i, k_i, ε_i
Valence Band
Core Level
Core Hole
Energy
ħω_o, k_o, ε_o
Valence Band
Core Level

Figure 3.3: Scheme of direct RIXS process: the incoming photon is absorbed and a deep-lying core electron is excited, creating an hole, to an empty state above the Fermi level. Due to the recombination between the valence electron and the core hole, the system is deexcites and there is an emission of a photon with energy equal to $\hbar\omega_i - \hbar\omega_o$. Figure taken from Ref. [56].

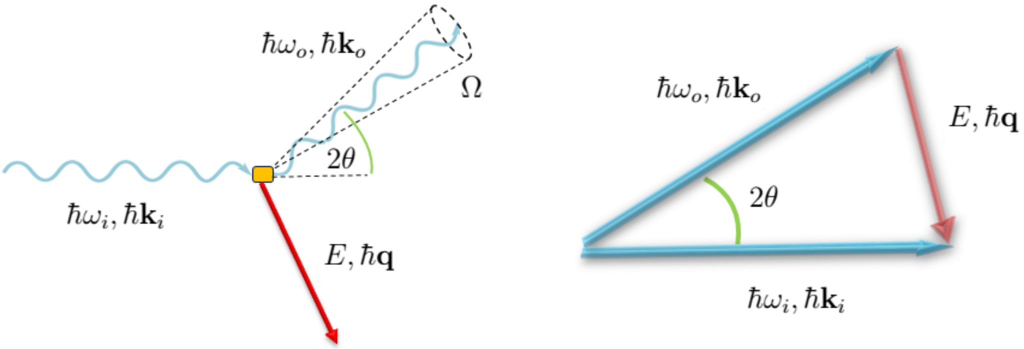
$\hbar\omega_o, \hbar\mathbf{k}_o$
Ω
2θ
$\hbar\omega_i, \hbar\mathbf{k}_i$
$E, \hbar\mathbf{q}$
$\hbar\omega_o, \hbar\mathbf{k}_o$
$E, \hbar\mathbf{q}$
2θ
$\hbar\omega_i, \hbar\mathbf{k}_i$

Figure 3.4: Scheme of the kinematic (left) and conservation laws (right) involved in RIXS process. E is the energy loss ($\hbar\omega_i - \hbar\omega_o$) of the scattered photon in a solid angle Ω after RIXS process, $\hbar\mathbf{q}$ ($\hbar\mathbf{k}_i - \hbar\mathbf{k}_o$) is the transferred momentum to a core electron of the sample and 2θ is the scattering angle defined by the scattering geometry.

3.3 RIXS cross-section

In this section we briefly report the theory of RIXS following the work done by Blume [57]. The starting point is to consider an ensamble of electrons interacting with a quantized electromagnetic field (described by the potential vector $\mathbf{A}(\mathbf{r},t)$) and a time-dependent perturbation. The total nonrelativistic Hamiltonian of the system, derived from QED, can be written as

$$\mathcal{H} = \sum_j \frac{1}{2m}\left(\mathbf{p}_j - \frac{e}{c}\mathbf{A}(\mathbf{r}_j)\right)^2 + \sum_{ij} V(\mathbf{r}_{ij}) + \\ -\frac{e\hbar}{2mc}\sum_j \mathbf{s}_j \cdot \nabla \times \mathbf{A}(\mathbf{r}_j) - \frac{e\hbar}{2(mc)^2}\sum_j \mathbf{s}_j \cdot E(\mathbf{r}_j) \times \left(\mathbf{p}_j - \frac{e}{c}\mathbf{A}(\mathbf{r}_j)\right) + \\ \sum_{\mathbf{k}\lambda} \hbar\omega_{\mathbf{k}}\left(c^\dagger_\lambda(\mathbf{k})c_\lambda(\mathbf{k}) + \frac{1}{2}\right) \tag{3.4}$$

where $E(\mathbf{r}) = -\nabla\phi - \frac{1}{c}\frac{\partial\mathbf{A}(\mathbf{r},t)}{\partial t}$ is the electric field of the electromagnetic radiation (ϕ describes the Coulomb potential), $c^\dagger_\lambda(\mathbf{k})$ and $c_\lambda(\mathbf{k})$ are the creation and annihilation operators ($\mathbf{k}$, λ are the quantum number of the photon created or annihilated), $\mathbf{s}_j$ and $\mathbf{p}_j$ are the spin and momentum operator of the j-th electron at the site $\mathbf{r}_j$.

We can notice that the first term of the total Hamiltonian in Eq. 3.4 is the kinetic energy of the electron considering the effect of the magnetic field of the radiation; the second term is the potential energy of the system; the third one is the Zeeman term while the fourth takes into account the effect of the spin-orbit interaction. These last two terms represent the interaction between the electron spin and the radiation field and finally, the fifth term corresponds to the radiation field. After these evaluations, and also considering that the vector potential $\mathbf{A}(\mathbf{r},t)$ can be expanded as a sum of plane waves, we can reformulate in a more simple way the Eq. 3.4:

$$\mathcal{H} = \mathcal{H}_{el} + \mathcal{H}_R + \mathcal{H}' \tag{3.5}$$

where $\mathcal{H}_{el}$ is the part of the total Hamiltonian that describes the unperturbed system which is the sum of the electronic Hamiltonians, $\mathcal{H}_R$ is the Hamiltonian relatives to the radiation and $\mathcal{H}'$ takes into account the interaction between photon and electron. The scattering process can thus be described as a transition between the eigenstates of $\mathcal{H}_{el}$ and $\mathcal{H}_R$ induced by the perturbation $\mathcal{H}'$.

Considering the scattering process between solid and X-rays beam, we assume that the solid is in an initial state $|a\rangle$, which is an eigenstate of $\mathcal{H}_{el}$ with energy E_a, and single photon is described by $|\mathbf{k}, \lambda\rangle$. The transition probability per unit of time induced by $\mathcal{H}'$ to a final state $|b\rangle$ plus a photon $|\mathbf{k}', \lambda'\rangle$ is given by the second order Fermi's "golden rule":

$$w = \frac{2\pi}{\hbar} \left| \langle f|\mathcal{H}'|i\rangle + \sum_n \frac{\langle f|\mathcal{H}'|n\rangle \langle n|\mathcal{H}'|i\rangle}{E_i - E_n} \right|^2 \delta(E_i - E_f) \tag{3.6}$$

where we consider the initial state of the system (X-ray photon and electron in the solid) described by $|i\rangle \equiv |a; \mathbf{k}, \lambda\rangle$ whereas $|f\rangle \equiv |b; \mathbf{k}', \lambda'\rangle$ describes the final state; index n runs over all possible intermediates states $|n\rangle$ that are eigenstates of the unperturbed Hamiltonian $\mathcal{H}_o = \mathcal{H}_{el} + \mathcal{H}_R$ with energies E_n. The dimension of w is [time^{-1}]. The first-order term in Eq. 3.6 was originally derived by Dirac, while the second-order term was obtained by Kramers and Heisenberg and today is usually called the *Kramers-Heisenberg* relation. The Kramers-Heisenberg relation gives the transition probability from an initial state $|i\rangle$ to a final state $|f\rangle$ via a range of virtual intermediate states $|n\rangle$. Energy conservation is ensured by the delta function involving the initial and final state energies. $|i\rangle$ and $|f\rangle$ are eigenstates of $\mathcal{H}_o$ with energies $E_i = E_a + \hbar\omega_{\mathbf{k}}$ and $E_f = E_b + \hbar\omega_{\mathbf{k}'}$. To proceed with the calculation of RIXS cross section, we rewrite the electric field as $\mathbf{E} = -\nabla\phi - \frac{1}{c}\frac{\partial \mathbf{A}}{\partial t}$. We obtain

$$\begin{aligned} \mathcal{H}' = {} & \frac{e^2}{2mc^2} \sum_j \mathbf{A}^2(\mathbf{r}_j) - \frac{e}{mc} \sum_j \mathbf{A}(\mathbf{r}_j) \cdot \mathbf{p}_j \\ & - \frac{e\hbar}{mc} \sum_j \mathbf{s}_j \cdot (\nabla \times \mathbf{A}(\mathbf{r}_j)) - \frac{e\hbar}{2(mc)^2} \frac{e^2}{c^2} \sum_j \mathbf{s}_j \cdot \frac{\partial \mathbf{A}(\mathbf{r}_j)}{\partial t} \times \mathbf{A}(\mathbf{r}_j) \\ & \equiv \mathcal{H}'_1 + \mathcal{H}'_2 + \mathcal{H}'_3 + \mathcal{H}'_4. \end{aligned} \tag{3.7}$$

As already mentioned, the number of photons is conserved during the scattering process and since **A** is linear in the creation and annihilation operators, the $\mathcal{H}'_1$ and $\mathcal{H}'_4$ terms contribute only to first order perturbation because they are quadratic in **A**, while $\mathcal{H}'_2$ and $\mathcal{H}'_3$ (linear in **A**) will contribute to the second order. Eq. 3.6 can therefore be recast in

$$w = \frac{2\pi}{\hbar}\Bigg| \langle f|\mathcal{H}'_1 + \mathcal{H}'_4|i\rangle + \\ + \sum_n \frac{\langle f|\mathcal{H}'_2 + \mathcal{H}'_3|n\rangle \langle n|\mathcal{H}'_2 + \mathcal{H}'_3|i\rangle}{E_a + \hbar\omega_{\mathbf{k}} - E_n}\Bigg|^2 \delta(E_a - E_b + \hbar\omega_{\mathbf{k}} - \hbar\omega_{\mathbf{k}'}). \tag{3.8}$$

The Inelastic X-ray Scattering (IXS) double differential cross-section then is

$$\frac{d^2\sigma}{d\Omega' dE'} = \frac{w\rho(E_f)}{I}, \tag{3.9}$$

where $\rho(E_f)$ is the density of final states and I the incident flux [58]. Since we are interested in the RIXS cross-section, we focus our attention on the second order term of Eq. 3.8, *e. g.* the resonant term. Also, we note that $\mathcal{H}'_3$ is negligible compared to $\mathcal{H}'_3$ and will therefore be neglected. Finally, we limit ourselves to the dipole approximations, *e. g.* when $|\mathbf{k}|$ is small enough that $\mathrm{e}^{i\mathbf{k}\cdot\mathbf{r}}$ is approximately constant at the length scale of the atomic wavefunctions. By doing so $\mathcal{H}'_2 = \mathbf{p}\cdot\mathbf{A}$ reduces to a term proportional to $\boldsymbol{\epsilon}\cdot\mathbf{r}$, which is usually called the dipole operator and indicated by $\mathcal{D}$. Then we have

$$w \propto \Bigg| \sum_n \frac{\langle f|\mathcal{D}_e^\dagger|n\rangle \langle n|\mathcal{D}_a|i\rangle}{E_i - \hbar\omega_{k_i} - E_n + i\Gamma_n}\Bigg|^2 \delta(E_i - E_f + \hbar\omega). \tag{3.10}$$

This equation represents the RIXS scattering transition probabiliy, in which $\langle f|\mathcal{D}_e^\dagger|n\rangle$ and $\langle n|\mathcal{D}_a|i\rangle$ are the matrix elements of radiative transition relative to the absorbed and emitted photons. The polarization dependence is included in the dipole operator $\mathcal{D}$. The imaginary term $i\Gamma_n$ is connected to the finite intermediate states linewidth. As discussed above, the summation is over all possible n intermediate states of the system that in a RIXS process are not directly experimentally observed and that allow for interference effects.

In Chapter 5.4 we describe the theoretical model and the results of the RIXS cross-sections calculations obtained using the single-ion model in the specific case of Iridates, while in Appendix A.1 we report in detail the results in two particular cases of interest, with the formulation in terms of atomic scattering tensor.

Chapter 4

Experimental setup

The main characteristics of the synchrotron radiation, the experimental instrumentations and layout of the ID20 beamline at the European Synchrotron Radiation Facility (ESRF, Grenoble) will be discussed in this chapter.

4.1 Synchrotron light source

A synchrotron is an extremely powerful source of X-rays and this occurs when a charge (electrons, protons, positrons) moving at relativistic speeds follows a curved trajectory [59]. In fact, when a moving electron changes direction, it emits energy and when the electron is moving fast enough (relativistic speed), the emitted energy is at X-rays wavelengths. Powerful electromagnets are used to focus and steer the beam inside a ring-shaped vacuum chamber, which minimises collisions with air molecules and allows storage of the beam at high energy levels for many hours. The peculiarity of the synchrotron radiation source is that it provides high collimated and intense light beams in a continuum spectral range from infra-red ($\sim$ 1 eV) up to hard X-rays ($\sim$ 100 keV).

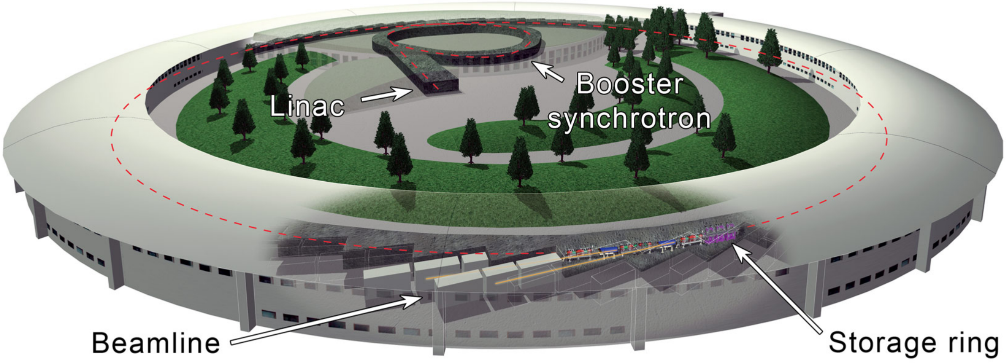

Figure 4.1: Schematic representation of a typical third-generation facility, in this case the ESRF. Figure taken from Ref. [60].

4.1.1 Synchrotron radiation at the ESRF

In a third-generation synchrotron light source, the electrons are produced by an electron gun, a device similar to the cathode ray tubes found in older televisions or computer screens. At ESRF [60] (shown in Fig. 4.1) these electrons are packed in bunches and then accelerated to 200 MeV by a linear accelerator (*linac*), and consequently they are injected into the booster synchrotron, a 300 m long circular accelerator in which the electrons are further accelerated via electric force in order to reach their final energy of about 6 GeV. Finally, the electrons enter in the storage ring, a 844 meter-long tube kept in very ultra high vacuum ($\sim 10^{-9}$ mbar), where they circulate at relativistic speed and pass through different types of magnets, emitting radiation used by the *beamlines* (the physical space within the experimental hall), each of them designed for use with a specific technique or for a specific type of research, connected to it. Inside the storage ring many structures are present, such as magnets and undulators (see Fig. 4.2). The ESRF storage ring includes 32 straight and 32 curved sections in alternating order. In each curved section, two large bending magnets force the path of the electrons into a circular orbit. In each straight section, several focusing magnets ensure that the electrons remain close to their ideal orbital path. The intense beam of X-

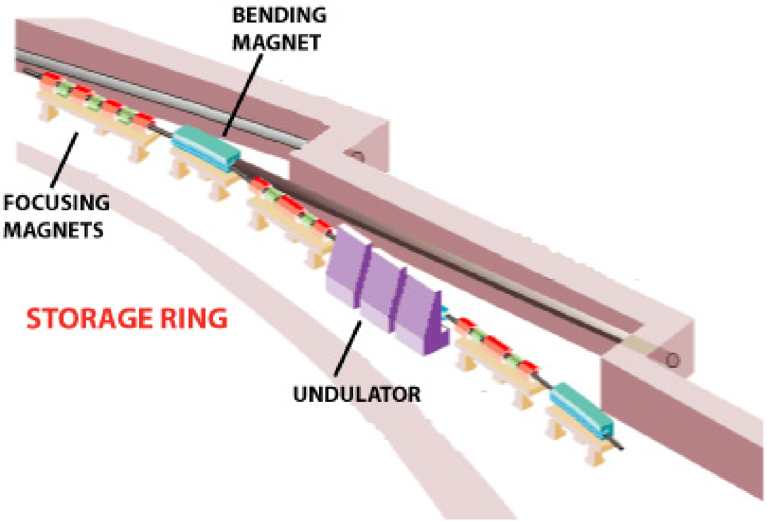

Figure 4.2: Design of the ESRF storage ring. Figure taken from Ref. [60].

rays is produced by the undulators, hosted in the straight sections of the ring, that are magnetic structures made up of a complex array of small magnets that force the electrons to follow an undulating, or wavy, trajectory. The radiation emitted at each consecutive bend overlaps and interferes with that from other bends. Undulator radiation has peculiar property, such as narrow spectral range, high photon flux, high brilliance and at the ESRF, the polarization is set linear horizontal. The gap between the rows of magnets can be changed to fine-tune the wavelength of the X-rays in the beam. Concerning bending magnets, their main function is to produce a magnetic field perpendicular to the plane of the ring that induces a Lorentz force making the path of the electrons circularly curved. The undulators are generally placed between two bending magnets and other electron beam optics.

4.2 ID20 beamline at the ESRF

The new ID20 beamline, constructed during Phase I of the ESRF Upgrade and operational since summer 2013, is a state-of-the-art Inelastic X-rays

Scattering (IXS). It is fully dedicated to the study of electronic excitations and provides two branches, one optimized for high detection efficiency and the other one for high energy resolution applications. This beamline operates in hard X-rays regime with incident photon energies ranging from 4 to 20 keV.

4.2.1 General optical layout

The overall optical layout of the beamline is shown in Fig. 4.3.

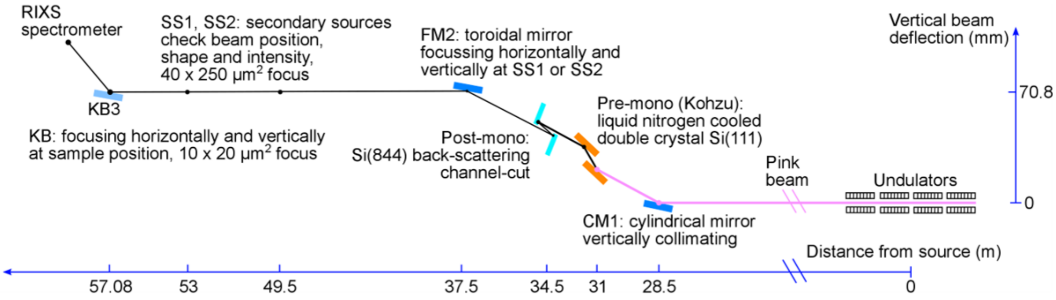
RIXS spectrometer
SS1, SS2: secondary sources check beam position, shape and intensity, 40 x 250 μm² focus
FM2: toroidal mirror focussing horizontally and vertically at SS1 or SS2
Vertical beam deflection (mm)
70.8
KB3
Pre-mono (Kohzu): liquid nitrogen cooled double crystal Si(111)
KB: focusing horizontally and vertically at sample position, 10 x 20 μm² focus
Post-mono: Si(844) back-scattering channel-cut
Pink beam
Undulators
0
CM1: cylindrical mirror vertically collimating
Distance from source (m)
57.08
53
49.5
37.5
34.5
31
28.5
0

Figure 4.3: Optical layout of the ID20 beamline. Figure elaborated from Ref. [61].

The X-rays used for experiments at ID20 beamline are generated by a 6 m long straight section equipped by four undulators with a periodicity of 26 mm. In order to collect, monochromatize and focus the X-rays at the sample position, there are many optical elements. After the undulators, the first optical component of the beamline is the collimating mirror (CM1), a vertically deflecting element. This element has a cylindrical shape and allows to reduce the X-rays beam power, collimate the beam in the vertical direction and reject the high order harmonics. The beam then goes through the Kohzu, a high heat load liquid-nitrogen Si(111) double crystal monochromator (DCM). DCM works at about the liquid-nitrogen temperature because it absorbs a significant fraction of the beam power. The energy selection is based on Bragg diffraction by the two Si(111) crystals, according to [62]

$$n\lambda = 2d \sin \theta_B \tag{4.1}$$

where $d = a_{Si}/\sqrt{h^2+k^2+l^2} = a_{Si}/\sqrt{3}$ (h, k and l are the Miller's indices and a_{Si}=5.43 Å) is the interatomic distance between lattice planes, λ is the wavelength of the incoming photons of the X-rays beam, θ_B is the Bragg angle and n is the diffraction order. The Bragg angle θ_B can be set in order to monochromatize the energy at the desired value according to the following relationship

$$\theta_B = \arcsin\left(\frac{\lambda}{2d}\right) = \arcsin\left(\frac{hc}{2dE_i}\right) \tag{4.2}$$

where h is the Planck's constant and c is the speed of light in vacuum.

Unlike Eq. 4.1 suggests, the response of these two crystals is not infinitely sharp in energy, but the reflection has an intrinsic width, which can be explained by the dynamical theory of diffraction. This width (called *Darwin* width) can be written as

$$\Delta\theta_{\mathrm{DW}} = \left(\frac{\Delta E}{E}\right)_{111} \tan\theta_{\mathrm{B}}. \tag{4.3}$$

Considering that the intrinsic energy resolution of the Si(111) reflection is $\left(\frac{\Delta E}{E}\right)_{111} \simeq 1.35\cdot 10^{-4}$, we have $\Delta E \simeq 1.5$ eV at an energy $E \simeq 11.215$ keV. For high resolution Ir L_3-edge RIXS experiments, the DCM is used in conjunction with a Si(844) channel-cut which operates in a close to back-scattering geometry. This post-monochromator improves the energy resolution to $\frac{\Delta E}{E}|_{844} = 1.3\cdot 10^{-6}$, *e. g.* $\Delta E = 15$ meV at 11.215 keV. The focusing mirror (FM2) is placed after the post-monochromator It is a vertically deflecting toroidal mirror with an adjustable radius of curvature that permit to focus the X-rays beam at the secondary sources SS1, which represent the source for the downstream optical elements, namely the Kirkpatrick-Baez mirrors (KB). KB mirrors permit to achieve a focal spot size along the horizontal and vertical direction in the order of 17×10 μm^2. After these optical elements, the incoming photon flux on the sample is in the order of 10^{12} photons/s.

4.2.2 The high-resolution IXS spectrometer

Once the X-rays beam is scattered by the sample, a spectrometer is used to analyse its energy. ID20 beamline is equipped with a spectrometer dedicated

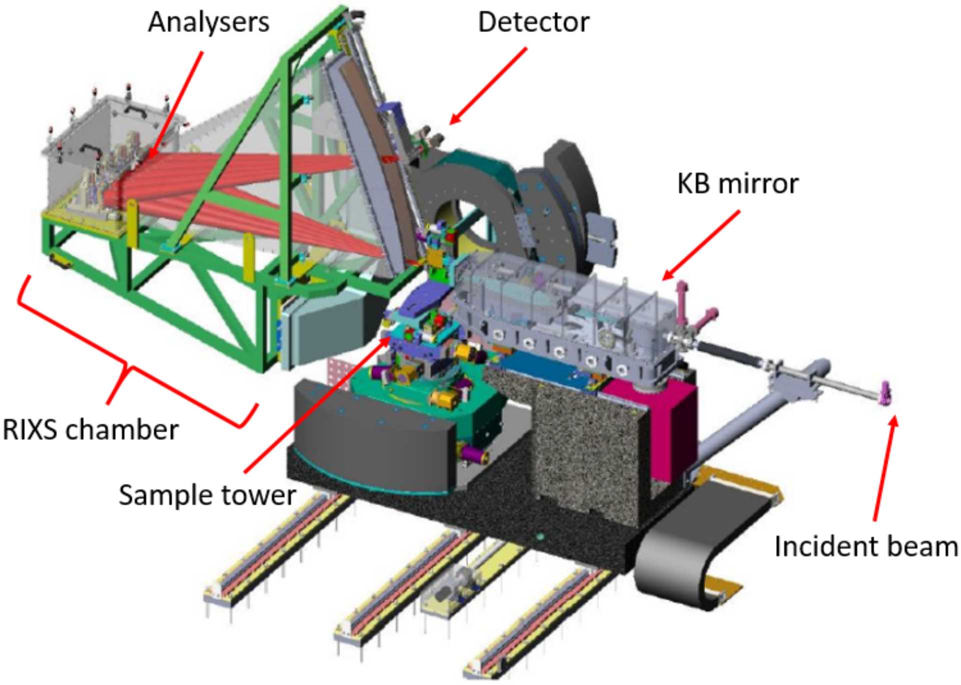

Figure 4.4: KB chamber and high-resolution IXS spectrometer.

to RIXS measurements shown in Fig. 4.4. It consists of a 2θ scattering arm which houses five crystal analysers. The analysers and the detector move on the Rowland circle (see Fig. 4.5) during a scattered photon energy scan. The detector is a pixelated Medipix. A He-filled chamber is used in order to reduce absorption and scattering by air. The so-called diced crystal spherical analysers are used at the Si(844) (shown on the right side of Fig. 4.5) and consist of a polygonal approximation to the spherical analysers.

One of the most important parameter of a RIXS spectrometer is energy resolution. The overall energy resolution depends, first of all, by the type of the analysers used and in case of diced crystal analysers it is well approximated by the intrinsic resolution of the reflection

$$\Delta E_a = E \left(\frac{\Delta E}{E} \right)_{844} \tag{4.4}$$

which amounts to 15 meV as in the case of the Si(844) post-monochromator. Another contribution is given by the so-called Johann aberrations caused by

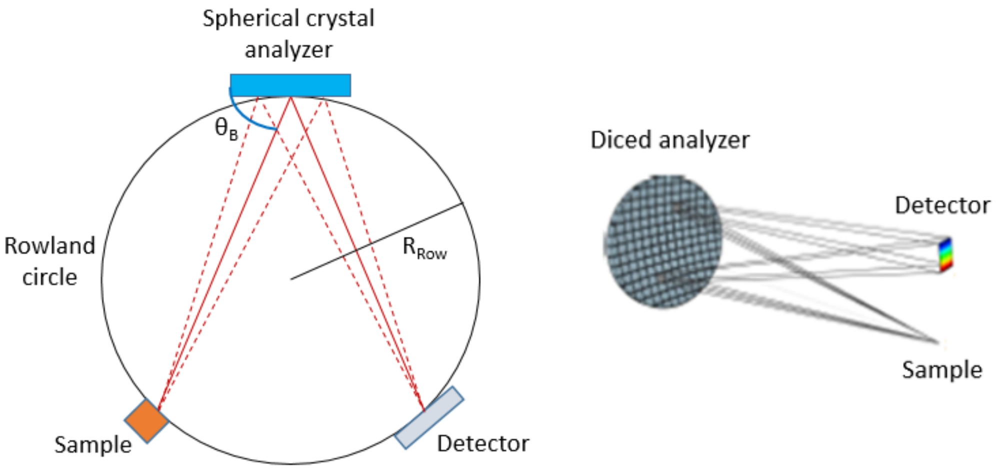

Figure 4.5: Position of the sample, analyser and dedector illustrated in a top view of the Rowland circle (on the left) and the diced analyser in detail (right).

a finite dispersion of Bragg angles across the surface of the analyser. If A is the aperture, we have the following contribution

$$\Delta E_j = \frac{E}{2}\left(\frac{A}{2R\tan\theta_B}\right)^2 \tag{4.5}$$

where $R = 2$ m is the diameter of the Rowland circle. For a typical mask size $A = 60$ mm, $\Delta E_j \approx 7$ meV. When diced crystal analysers are used, a distribution of photon energies across the detector surface is produced. Another contribution to the energy resolution is, then, given by how finely his distribution of photon energies is sampled and directly depends on the detector pixel size p according to

$$\Delta E_p = E\frac{\Delta\theta_p}{\tan\theta_B} \tag{4.6}$$

where $\Delta\theta_p = p/2\sin\theta_B$. In our case, $p = 55$ μm and $\Delta E_p = 11$ meV. The last contribution is given by the focal spot size at the sample which acts as a source for the spectrometer. The finite source size s introduces a residual divergence $\Delta\theta_s = s/(R\sin\theta_B)$ that gives the following contribution

$$\Delta E_s = E\frac{\Delta\theta_s}{\tan\theta_B}. \tag{4.7}$$

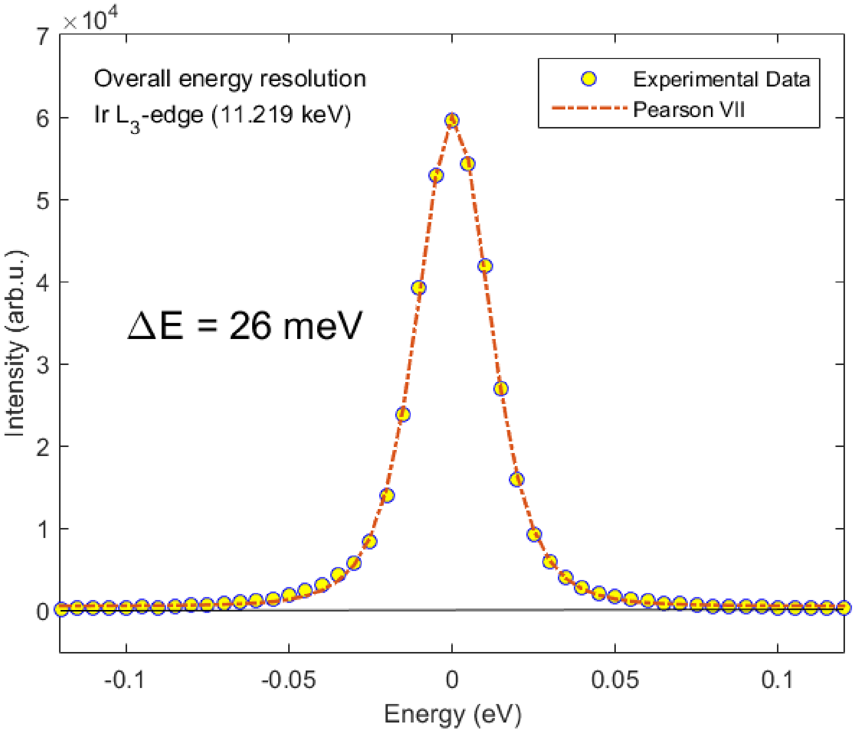

Figure 4.6: Measured elastic peak on a polymer sample in order to calculate the instrumental energy resolution. The red dashed line is a fit to a Pearson VII function of FWHM = 26 meV.

In our case, $s = 10$ μm and $\Delta E_s = 4$ meV. Adding quadratically all these contributions ($\Delta E_0 = \sqrt{\Delta E_a^2 + \Delta E_j^2 + \Delta E_p^2 + \Delta E_s^2}$) we can estimate the resolution of the RIXS spectrometer to be $\Delta E_0 \sim 20$ meV. This adds to the incident photon energy resolution of 15 meV to an overall energy resolution of approximately 25 meV. Experimentally, the energy resolution of the beamline plus spectrometer is obtained measuring the elastic line of a polymer. In Fig. 4.6 the experimental curve is fitted by a Pearson VII distribution (see Eq. 5.1) where the corresponding full-width at half-maximum (FWHM) is $\Delta E = 26$ meV, in agreement with the calculated one.

Regarding the momentum resolution of the RIXS spectrometer, this is mainly defined by the angular acceptance of the crystal analysers, A. Considering an analyser diameter of $A = 40$ mm and a $R = 2$ m spectrometer the angular acceptance is $\Delta\theta' = A/R \sin\theta_B \approx 1^\circ$. Considering that $|\mathbf{q}| = 2|\mathbf{k}| \sin\theta$, the uncertainty on the modulus of the momentum transfer is $|\Delta\mathbf{q}| = 2|\mathbf{k}| \cos\theta\Delta\theta \approx 0.28$ Å^{-1} at $2\theta = 90^\circ$.

Chapter 5

Iridium fluorides

In this chapter we report a series of RIXS measurements and their interpretation in a number of iridium fluorides. We develop the calculation of RIXS cross-sections based on a single ion model and extract effective parameters for the crystal field splitting and spin-orbit coupling by comparison with the experiments.

5.1 Motivation for this work

Following the theoretical prediction of possible high-temperature superconductivity in undistorted (SU(2) symmetric) $J_{\text{eff}} = 1/2$ insulators when electron-doped [1], many studies have been carried out in order to identify new compounds that could host such a ground state. Recently, Birol *et al.* [5] suggested that Rb_2RhF_6 and Rb_2IrF_6 may display an undistorted $J_{\text{eff}} = 1/2$ ground state based on density functional theory (DFT) and dynamical field theory (DMFT).

The space group of Rb_2IrF_6 is trigonal $P\bar{3}m1$ (Fig. 5.1(a)). While there is no symmetry element that imposes the IrF_6 octahedra to be regular, all six Ir-F bond lengths are equal and the F-Ir-F angles are close to 90°, as in K_2GeF_6 (KGF structure that is shown in Fig. 5.1(b))[63, 64]. In addition, unlike in Sr_2IrO_4 where the apical and in-plane oxygens are coordinated

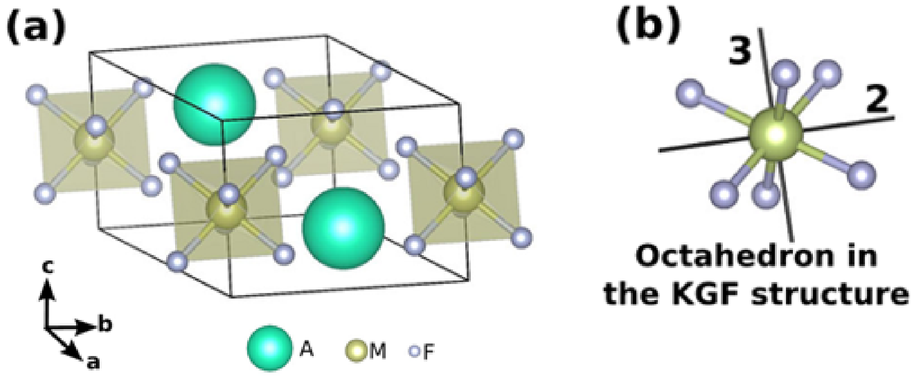

Figure 5.1: a) Crystal structure of compounds with chemical formulae A_2IrF$_6$, *e. g.* K$_2$GeF$_6$ (KGF)-type, where A is the alkali metal ion. Ir is at the center of the IrF$_6$ octahedron and all ligands are symmetry and chemically equivalent. b) Coordination environment of the transition metal in the KGF structure. Figure taken from Ref. [5].

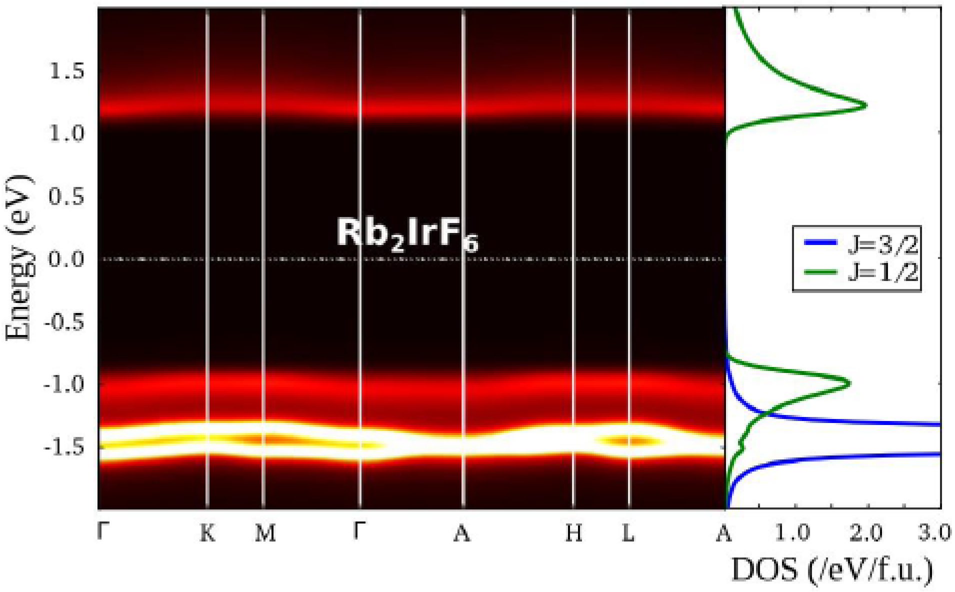

Figure 5.2: Spectral function and DOS of Rb$_2$IrF$_6$ as given by DFT calculations. Figure taken from Ref. [5].

differently, in Rb_2IrF_6 all ligands are symmetry equivalent and as a result an equally distorted ochtahdron is expected to cause a smaller splitting of the $5d$-t_{2g} states compare to Sr_2IrO_4. Finally, the IrF_6 octahedra are isolated (in the sense that there are no F ligands coordinated to two different Ir ions), the effective hopping between the Ir ions is small and hence the $5d$-t_{2g} bands at the Fermi level are expected to be extremely narrow, rendering the system a strong Mott insulator.

Fig. 5.2 shows DFT and DMFT calculations of Rb_2IrF_6. Indeed, they predict an insulating state with a band gap larger than 2 eV and almost dispersionless bands. Orbital character analysis of the density of states shows that the bands above and right below the Fermi level are mainly composed of $J_{\text{eff}} = 1/2$-like states, in analogy to the case of Sr_2IrO_4.

The aim of our RIXS measurements is to characterize the ground and excited states of Rb_2IrF_6 and other iridium fluorides, possibly quantify the crystal field and the SOC energy scales, and compare the experiments with the above theoretical predictions.

5.2 Expermental details

RIXS experiments were performed on a few mg powders of A_2IrF_6 (where A=Li, Na, K, Rb and Cs are the alkali metals) and $BIrF_6$ (where B=Sr and Ba are alkaline earth metals). The scattering angle for all measurements was fixed at $2\theta = 90°$ with the beam hitting the sample surface at $\theta_{inc} = 45°$, *e. g.* in a specular scattering geometry. The polarisation of incident photon beam is parallel to the scattering plane and horizontal in the laboratory reference frame.

Fig. 5.3 shows a low energy resolution RIXS map ($\Delta E \approx 350$ meV) of Rb_2IrF_6 for incident photon energies ranging from 11.217 to 11.224 keV, thus spanning across the Ir L_3-edge (see Fig. 5.4). The XAS spectrum is essentially featureless as all the details of the electronic multiplet structure are washed out by the large core-hole lifetime broadening. The RIXS map,

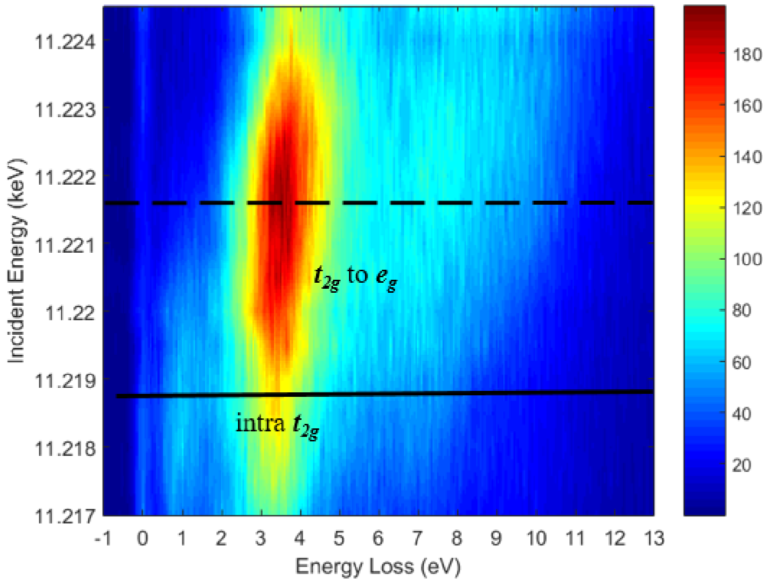

Figure 5.3: Incident energy dependence of Ir L_3-edge RIXS spectra measured on Rb_2IrF_6 powder sample at 300 K. The continuous and dashed black lines show the resonance energies of the t_{2g} and e_g states at 11.219 and 11.222 keV, respectively.

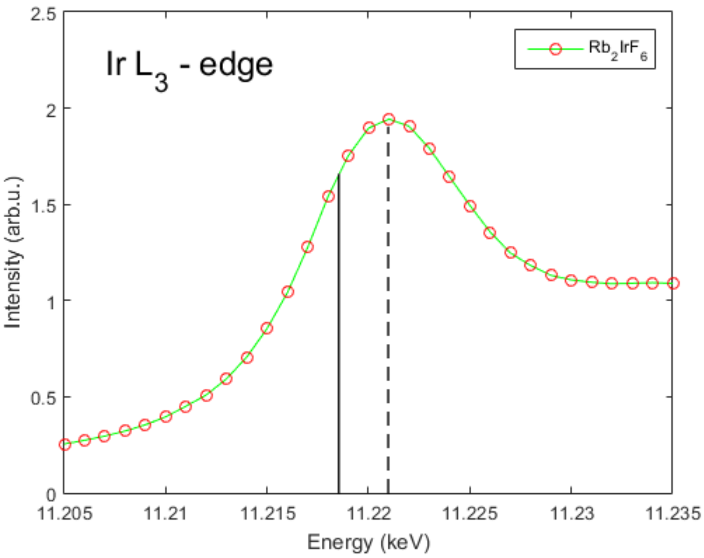

Figure 5.4: Ir L_3-edge XAS spectrum of Rb_2IrF_6. The continuous and dashed black lines show the resonance energies of the t_{2g} and e_g states at 11.219 and 11.222 keV, respectively, as in Fig. 5.3.

instead, is rich and shows several features: the elastic line at zero energy loss and excitations at about 1, 4 and 8 eV. They all have a clear resonant behaviour, although with a different resonance photon energy. In particular the 4 and 8 eV features resonates at the maximum of the absorption edge, whereas the 1 eV feature resonates approximately 3 eV below. This behaviour is quite common in iridates and allows us to assign the 1 eV and the 4 eV features to intra–t_{2g} and t_{2g}–to–e_g, respectively. The 8 eV feature, instead, likely corresponds to charge-transfer excitations.

Since we are particularly interested in the nature of the $5d$–t_{2g} states, we fixed the incident photon energy at 11.219 keV and further investigated the low energy feature with the high energy resolution setup ($\Delta E = 26$ meV, see Chapter 4.2.2 and Fig. 4.6).

Fig. 5.5 shows the RIXS spectrum of $\mathrm{Rb_2IrF_6}$ obtained at room temperature. The spectrum shows that the 1 eV feature is split in two distinct peaks, labelled A and B. The spectrum was fitted using a Pearson VII-type function, whose analytical equation is

$$p(x) = \frac{A}{\left[1 + \left(2^{\frac{1}{\mu}} - 1\right)\left(2\frac{x-x_0}{\sigma}\right)^2\right]^{\mu}} \tag{5.1}$$

where A is the amplitude, x_0 is the center of the peak, σ is the full width at half maximum (FWHM) and μ is a parameter that controls the shape of the curve: for $\mu = 1$ it reduces to a Lorentzian profile, while for $\mu \to \infty$ it approaches a Gaussian profile.

The two peaks A and B are found at 0.83 and 0.94 eV, respectively. As already mentioned, these peaks are assigned to intra–t_{2g} excitations and their splitting is indicative of a sizeable contribution of the trigonal crystal field. On the other hand, if the crystal field was perfectly octahedral, we should expect only one peak, corresponding to the transition from the $J_{\mathrm{eff}} = 1/2$ ground state to the degenerate $J_{\mathrm{eff}} = 3/2$ excited states. A quantitative estimate of the trigonal crystal field splitting will be given in the following. The center of mass of the two peaks is, instead, mostly dictated by the strength of the spin-orbit coupling, as suggested by Fig. 2.2.

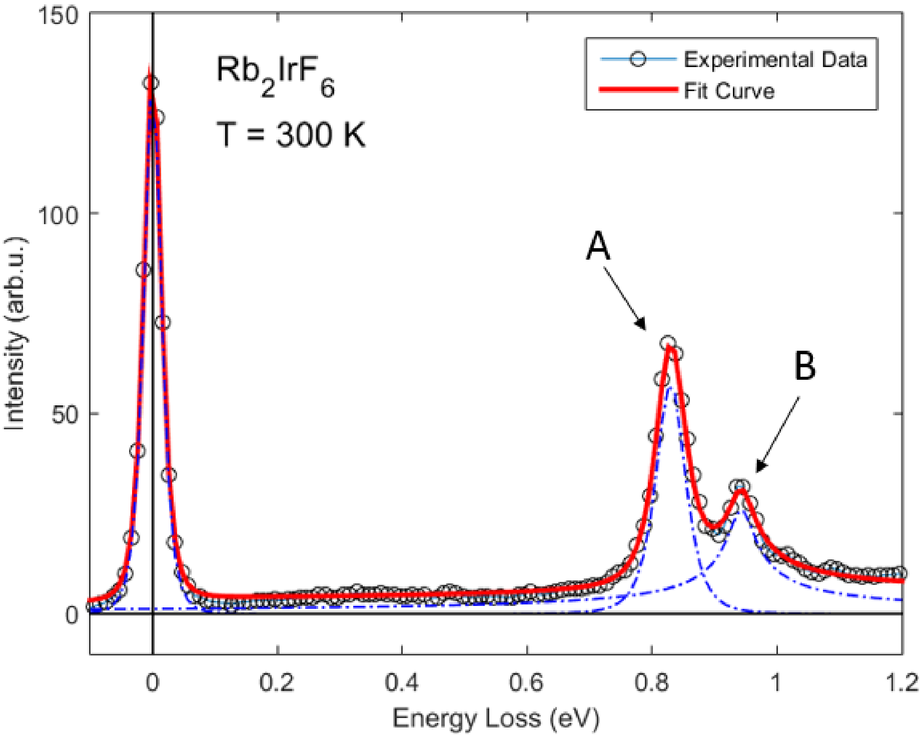

Figure 5.5: High resolution RIXS spectrum of Rb_2IrF_6 powder sample obtained with E_i=11.219 keV at 300 K. Open circles represent the experimental data, the red line is the total fit and the dashed blue lines are the fit to features A and B.

Fig. 5.6 shows the high energy resolution RIXS spectra of the other iridium fluorides. We note that the incident photon energy was kept the same for all compounds as the corresponding XAS are very similar (not shown). Strikingly, all RIXS spectra show a splitting of the intra–t_{2g} excitations, similar to the case of Rb_2IrF_6. The precise value of the splitting varies among the different samples and is largest for Na_2IrF_6, but in any case the low energy peak (A in Fig. 5.5) is more intense than the high energy peak (B in Fig. 5.5). Fig. 5.6 also shows the temperature change of the RIXS spectra between 300 and 10 K: while the spectra still look qualitatively similar to the room temperature case, the temperature effect is very sample dependent and is the most pronounced in Na_2IrF_6. On the other hand, the center of mass of the peaks is roughly the same in all compounds and shows little temperature dependence, implying a

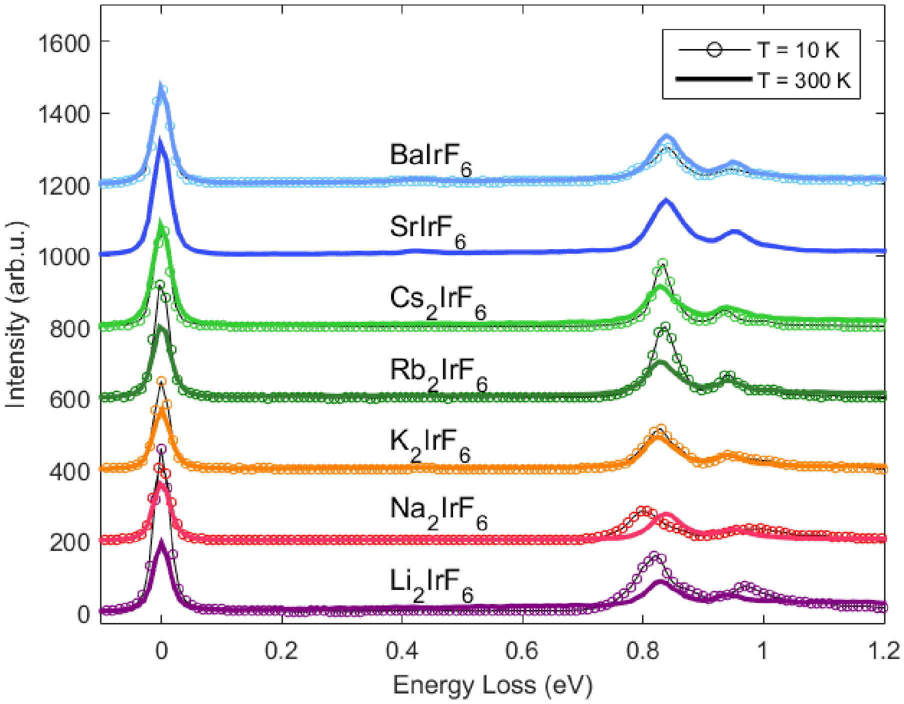

Figure 5.6: RIXS spectra of various iridium fluorides at 10 (open circles) and 300 K (continuos line).

	A		**B**		**B-A**		**(A+B)/2**	
	300 K	10 K	300 K	10 K	300 K	10 K	300 K	10 K
Li_2IrF_6	0.829	0.823	0.939	0.976	0.111	0.15	0.884	0.898
Na_2IrF_6	0.838	0.805	0.951	0.988	0.113	0.185	0.895	0.896
K_2IrF_6	0.826	0.823	0.943	0.938	0.117	0.115	0.885	0.881
Rb_2IrF_6	0.831	0.835	0.943	0.938	0.115	0.109	0.877	0.889
Cs_2IrF_6	0.829	0.832	0.938	0.938	0.109	0.106	0.885	0.885
$SrIrF_6$	0.839	-	0.954	-	0.115	-	0.896	-
$BaIrF_6$	0.840	0.842	0.953	0.942	0.114	0.111	0.896	0.898

Table 5.1: Results of the fitting to the spectra of Fig. 5.6. A and B are the peak positions, (B-A) their splitting and (B+A)/2 their center of mass at 10 and 300 K.

similar value of the spin-orbit constants in all compounds, as expected. A summary of the energies of peaks A and B, their splitting (B-A) and the corresponding center of mass (B+A)/2 for the various samples is given in Tab. 5.1.

We investigated in detail the temperature dependence of the RIXS spectra of Na_2IrF_6, shown in Fig. 5.7(a).

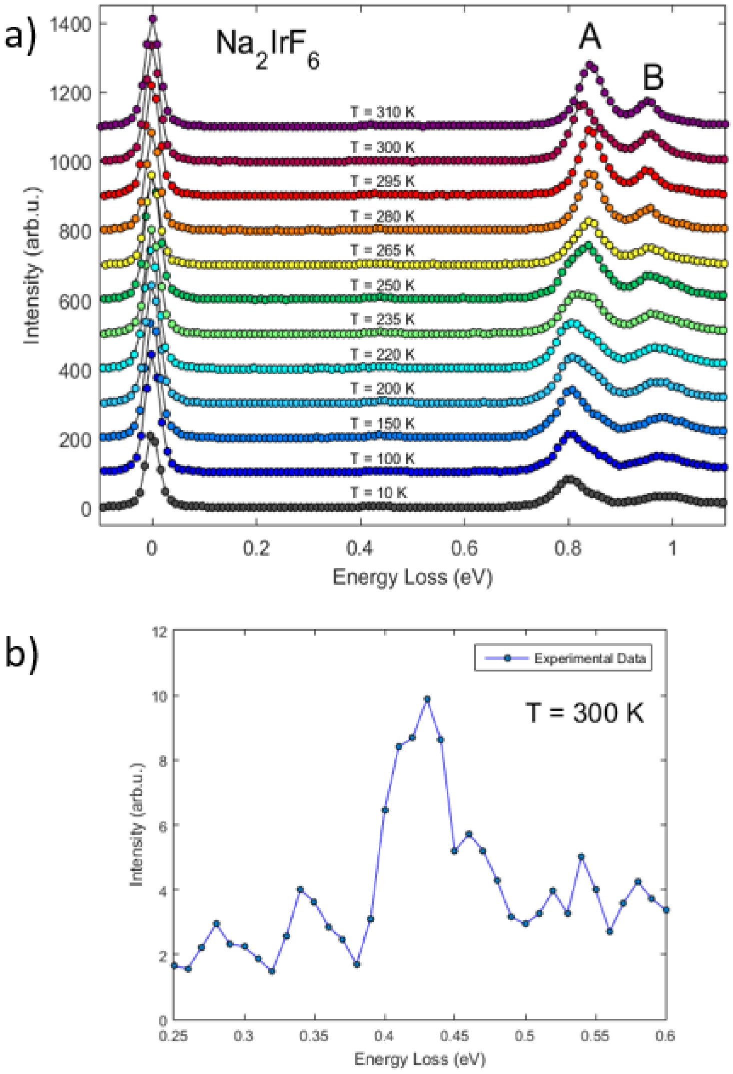

Figure 5.7: a) Temperature dependence of *d*-*d* excitations in Na_2IrF_6. b) Zoom on the low energy (~ 0.43 eV) feature at 300 K.

In this sample, the temperature evolution of intra–t_{2g} excitations is very pronounced and the splitting increases when the temperature is lowered, with the largest changes occurring in the temperature range between 200 and 300 K. It is interesting to note that this behaviour is markedly different than in the case of iridium oxides where no temperature change has been reported for intra–t_{2g} excitations.

Finally, we highlight in Fig. 5.7(b) a weak feature at about 0.43 eV. This peak is poorly temperature dependent and is observed also in K_2IrF_6, Rb_2IrF_6, $SrIrF_6$ and $BaIrF_6$. It closely resembles peaks observed in other iridium oxides and whose assignment is still matter of debate [6, 18, 65], so it will not be discussed further.

The next step is to carry out a quantitative analysis of the RIXS spectra by extracting effective parameters for the crystal field splitting and spin-orbit coupling. In order to do so, in the following we solve a single ion Hamiltonian including trigonal (in the case of K_2IrF_6, Rb_2IrF_6, Cs_2IrF_6, $SrIrF_6$ and $BaIrF_6$ or tetragonal (in the case of Na_2IrF_6 and Li_2IrF_6) crystal field splitting and spin-orbit coupling. However, it will be soon clear that the comparison with the experiments allows for two different solutions with opposite signs of the trigonal/tetragonal crystal field splitting. In order to distinguish among the two cases, we develop the calculation of the RIXS cross-sections and notice that the RIXS intensities of only one of the two solutions fit the data consistently.

5.3 Single-ion model Hamiltonian

As explained above, in order to get a better insight into the electronic structure of iridium fluorides, in particular Rb_2IrF_6, we adopt a single ion model and solve a simple Hamiltonian including trigonal crystal field splitting and spin-orbit coupling. The case of tetragonal crystal field splitting follows along similar lines and will not be treated in detail.

The first observation is that Ir is oxidised 4+, that is we are dealing with

5 electrons occupying the $5d$–t_{2g} states (e_g are neglected because far off in energy, see Chapter 2.2). Equivalently, one can consider one *hole*. Dealing with one particle greatly simplifies the treatment because particle-particle interaction are absent. This allows us to develop a simple Hamiltonian, which can be constructed and diagonalised in the basis set of Hydrongen-like wavefunctions

$$\Psi_{n,l,m}(r,\theta,\phi) = R_n^l(r)Y_l^m(\theta,\phi). \tag{5.2}$$

In the following, we will neglect the radial part of the wavefunctions and deal with the angular part only, represented by spherical harmonics Y_l^m, as this is the one which is affected by crystal field and spin-orbit coupling. For d states, the angular momentum is $l = 2$ and the magnetic quantum number is $m = -2, -1, 0, 1, 2$. When the symmetry of the problem is spherical, all these states are degenerate. On the other hand, when the symmetry is lowered, the degeneracy is lifted. For octahedral crystal field symmetry, d states split in e_g states

$$d_{x^2-y^2} = \frac{1}{\sqrt{2}}(Y_2^{-2} + Y_2^2) \tag{5.3a}$$

$$d_{3z^2-r^2} = Y_2^0 \tag{5.3b}$$

and t_{2g} states

$$d_{xy} = \frac{i}{\sqrt{2}}(Y_2^{-2} - Y_2^2) \tag{5.4a}$$

$$d_{yz} = \frac{i}{\sqrt{2}}(Y_2^{-1} + Y_2^1) \tag{5.4b}$$

$$d_{xz} = \frac{1}{\sqrt{2}}(Y_2^{-1} - Y_2^1) \tag{5.4c}$$

which are expressed here as linear combination of Y_l^m. When considering a trigonal distortion (elongation or compression along the [1 1 1] axis), e_g and t_{2g} states are further split. From now on, we will focus on the t_{2g} states only and write [66]

$$t_{2g}^0 = d_{3z^2-r^2} \tag{5.5a}$$

$$t_{2g}^+ = \sqrt{\frac{2}{3}}d_{x^2-y^2} - \sqrt{\frac{1}{3}}d_{xy} \tag{5.5b}$$

$$t_{2g}^{-} = \sqrt{\frac{2}{3}}d_{xy} + \sqrt{\frac{1}{3}}d_{yz} \tag{5.5c}$$

which we choose as our basis set. The single ion Hamiltonian we consider [45] is

$$\mathcal{H} = \mathcal{H}^{SOC} + \mathcal{H}^{CF} = \zeta\mathbf{L}\cdot\mathbf{S} + \Delta_{tri}\left(\frac{2}{3}\left|t_{2g}^{0}\right\rangle\left\langle t_{2g}^{0}\right| - \frac{1}{3}\left|t_{2g}^{\pm}\right\rangle\left\langle t_{2g}^{\pm}\right|\right) \tag{5.6}$$

where ζ is the spin-orbit coupling term and Δ_{tri} is the trigonal crystal field splitting. $\mathcal{H}^{CF}$ is obviously diagonal in the chosen basis

$$\underline{\mathcal{H}}^{CF} = \frac{\Delta_{tri}}{3}\begin{pmatrix} 2 & 0 & 0 & 0 & 0 & 0 \\ 0 & 2 & 0 & 0 & 0 & 0 \\ 0 & 0 & -1 & 0 & 0 & 0 \\ 0 & 0 & 0 & -1 & 0 & 0 \\ 0 & 0 & 0 & 0 & -1 & 0 \\ 0 & 0 & 0 & 0 & 0 & -1 \end{pmatrix} \tag{5.7}$$

since

$$\left\langle t_{2g}^{0}\right|\mathcal{H}^{CF}\left|t_{2g}^{0}\right\rangle = \frac{2}{3}\Delta_{tri} \tag{5.8a}$$

$$\left\langle t_{2g}^{\pm}\right|\mathcal{H}^{CF}\left|t_{2g}^{\pm}\right\rangle = -\frac{1}{3}\Delta_{tri}. \tag{5.8b}$$

$\mathcal{H}^{SOC}$ is easily calculated in the basis set of spherical harmonics considering that [67]

$$\mathcal{H}^{SOC} = \zeta\mathbf{L}\cdot\mathbf{S} = \zeta\left(L_z S_z + \frac{1}{2}(L^{+}S^{-} + L^{-}S^{+})\right) \tag{5.9}$$

where the ladder operators for both the angular and spin momentum are defined as

$$J_{\pm}\left|j, m_j\right\rangle = \sqrt{j(j+1) - m_j(m_j \pm 1)}\left|j, m_j \pm 1\right\rangle \tag{5.10a}$$

$$J_z\left|j, m_j\right\rangle = \left|j, m_j\right\rangle \tag{5.10b}$$

and then applying a basis transformation from spherical harmonics to the basis defined in Eq.5.5. By doing so, we obtain

$$\underline{\mathcal{H}}^{SOC} = \frac{\zeta}{2} \begin{pmatrix} 0 & 0 & 0 & 1 & 0 & i \\ 0 & 0 & -1 & 0 & i & 0 \\ 0 & -1 & 0 & 0 & -i & 0 \\ 1 & 0 & 0 & 0 & 0 & i \\ 0 & -i & i & 0 & 0 & 0 \\ -i & 0 & 0 & -i & 0 & 0 \end{pmatrix}. \tag{5.11}$$

Taking into account the simultaneous action of $\mathcal{H}^{SOC}$ and $\mathcal{H}^{CF}$ we obtain

$$\underline{\mathcal{H}} = \begin{pmatrix} \frac{2\Delta_{tri}}{3} & 0 & 0 & \frac{\zeta}{2} & 0 & \frac{i\zeta}{2} \\ 0 & \frac{2\Delta_{tri}}{3} & -\frac{\zeta}{2} & 0 & \frac{i\zeta}{2} & 0 \\ 0 & -\frac{\zeta}{2} & -\frac{\Delta_{tri}}{3} & 0 & -\frac{i\zeta}{2} & 0 \\ \frac{\zeta}{2} & 0 & 0 & -\frac{\Delta_{tri}}{3} & 0 & \frac{i\zeta}{2} \\ 0 & -\frac{i\zeta}{2} & \frac{i\zeta}{2} & 0 & -\frac{\Delta_{tri}}{3} & 0 \\ -\frac{i\zeta}{2} & 0 & 0 & -\frac{i\zeta}{2} & 0 & -\frac{\Delta_{tri}}{3} \end{pmatrix} \tag{5.12}$$

which can then be diagonalised to obtain the eigenvectors

$$|0,\pm\rangle = \frac{-A\,|t_{2g}^{0},\pm\rangle \mp |t_{2g}^{+},\mp\rangle + i\,|t_{2g}^{-},\mp\rangle}{\sqrt{2+A^2}} \tag{5.13a}$$

$$|1,\pm\rangle = \frac{B\,|t_{2g}^{0},\pm\rangle \mp |t_{2g}^{+},\mp\rangle + i\,|t_{2g}^{-},\mp\rangle}{\sqrt{2+B^2}} \tag{5.13b}$$

$$|2,\pm\rangle = \frac{\pm\,|t_{2g}^{+},\mp\rangle + i\,|t_{2g}^{-},\mp\rangle}{\sqrt{2}} \tag{5.13c}$$

which are so-called *Kramers doublets*. The effect of the trigonal crystal field splitting and spin-orbit coupling is encoded in the two terms $A = \frac{\sqrt{4\Delta_{tri}^2-4\Delta_{tri}\zeta+9\zeta^2}+2\Delta_{tri}-\zeta}{2\zeta}$ and $B = \frac{\sqrt{4\Delta_{tri}^2-4\Delta_{tri}\zeta+9\zeta^2}-2\Delta_{tri}+\zeta}{2\zeta}$. The corresponding eigenvalues are

$$E_0 = \frac{\zeta}{12}\left(\delta+3+3\sqrt{\delta(\delta-2)+9}\right) \tag{5.14a}$$

$$E_1 = \frac{\zeta}{12}\left(\delta+3-3\sqrt{\delta(\delta-2)+9}\right) \tag{5.14b}$$

$$E_2 = -\frac{\zeta}{6}\left(3+\delta\right), \tag{5.14c}$$

where $\delta = \frac{2\Delta_{tri}}{\zeta}$ and these are shown in Fig. 5.8(a) as a function of Δ_{tri}.

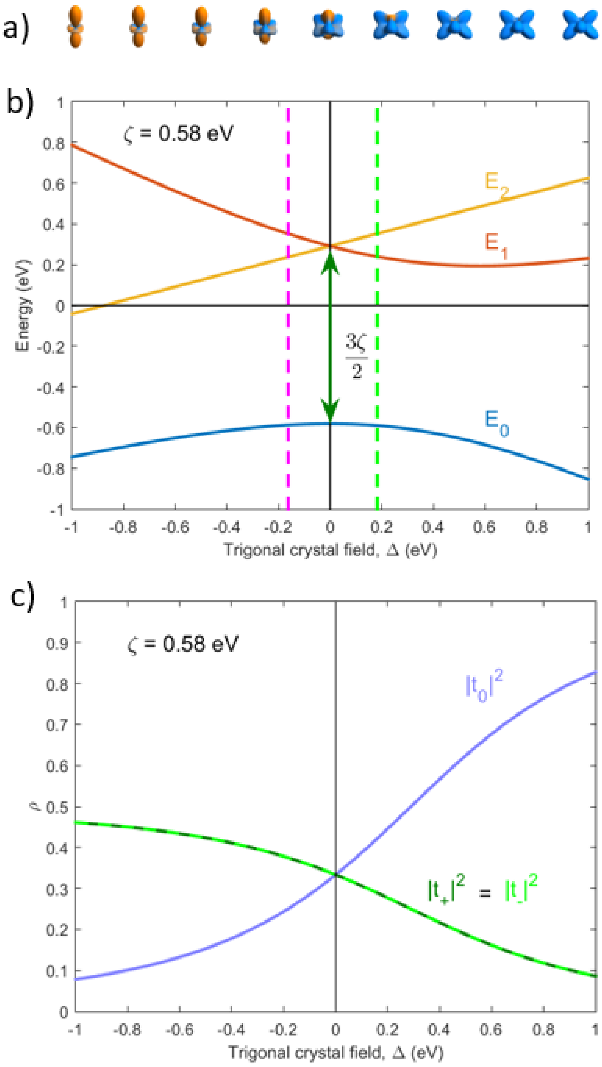

Figure 5.8: a) Real space representation of the ground state wavefucntion as a function of trigonal crystal field splitting. b) Dependence of the eigenvalues (Eq. 5.14) on the effective trigonal crystal field splitting Δ_{tri} for a spin-orbit coupling of $\zeta = 0.58$ eV. Pink and green dashed lines correspond to the two solutions ($\Delta_{tri} = 0.183$ and $\Delta_{tri} = -0.162$ eV), that equally well reproduce the splitting of the RIXS spectrum of Rb_2IrF_6 as explained in Chapter 5.5. c) Dependence of the orbital occupancies on the effective trigonal crystal field splitting Δ_{tri} for a spin-orbit coupling of $\zeta = 0.58$ eV.

The ground state is represented by the lowest energy state, *e. g.* $|0,\pm\rangle$ at all values of Δ_{tri}. For $\Delta_{tri} = 0$ we see that the $|1,\pm\rangle$ and $|2,\pm\rangle$ states merge in a quartet, the so-called $J_{\text{eff}} = 3/2$ quartet, and the ground state $|0,\pm\rangle$ reduces to the $J_{\text{eff}} = 1/2$ ground state. Their energy separation is $\frac{3\zeta}{2}$. At finite values of Δ_{tri}, all the three Kramers doublet are split in energy.

Within this picture, one can interpret RIXS excitations as transitions of the hole from the $|0,\pm\rangle$ ground state to either the $|1,\pm\rangle$ or the $|2,\pm\rangle$ excited states. It is therefore clear that the mere observation of two peaks in the RIXS spectrum in Fig. 5.5 can only be interpreted as due to a finite contribution of the trigonal crystal field splitting. However, nothing can be said about the sign of Δ_{tri}, as one can find solutions with either a positive or a negative value of Δ_{tri} that reproduce the splitting observed experimentally, as shown in Fig. 5.8.

In Fig. 5.8(b), instead, we report the trigonal crystal field dependence of the ground state orbital occupancies: for $\Delta_{tri} = 0$ the ground state is characterized by an equal admixture of $|t^0_{2g}\rangle$, $|t^+_{2g}\rangle$ and $|t^-_{2g}\rangle$ orbitals, as expected. A real space visualization of the ground state eigenfunction is reported at the top of Fig. 5.8(b).

5.4 Single-ion RIXS cross-section (trigonal case)

In this section we calculate the RIXS cross-sections in the single-ion model following the treatment adopted by M. Moretti Sala *et al.* in the case of cuprates [16] and in case of tetragonally distorted iridates [30]. The aim is to calculate the dependence of the RIXS cross-section on the trigonal crystal field splitting and try to fix the sign of Δ_{tri} by comparison with the measured intensities.

RIXS is a second order process and is described by the Kramers-Heisenberg equations (Eq. 3.10); we report here a simpler form for the scattering amplitude

$$\mathcal{A}^{\epsilon\epsilon'}_{|f,\pm\rangle} \propto \sum_n \langle f|\mathcal{D}^\dagger_e|n\rangle \langle n|\mathcal{D}_a|i\rangle \tag{5.15}$$

where we have assumed the same lifetime ($\Gamma_n = \Gamma$) for all $|n\rangle$ intermediate states at a given absorption edge ($E_n = E$). $\boldsymbol{\epsilon}$ and $\boldsymbol{\epsilon}'$ define the polarisation of the incoming and outgoing photons. As described in Chapter 3.3, the electric dipole operator can be written as $\mathcal{D} = \boldsymbol{\epsilon} \cdot \mathbf{r}$. It is useful to write it in spherical harmonics as

$$\begin{aligned}\boldsymbol{\epsilon} \cdot \mathbf{r} &= \boldsymbol{\epsilon}_x \sin\theta \cos\phi + \boldsymbol{\epsilon}_y \sin\theta \sin\phi \ + \boldsymbol{\epsilon}_z \cos\theta \\ &= \sqrt{\frac{4\pi}{3}} \left(\boldsymbol{\epsilon}_z Y_1^0 + \frac{-\boldsymbol{\epsilon}_x + i\boldsymbol{\epsilon}_y}{\sqrt{2}} Y_1^1 + \frac{\boldsymbol{\epsilon}_x + i\boldsymbol{\epsilon}_y}{\sqrt{2}} Y_1^{-1} \right). \end{aligned} \tag{5.16}$$

In the specific case of RIXS at the Ir L_3-edge, the transitions involved are: $2p^4_{\frac{3}{2}} 5t^5_{2g}$ (initial state) $\rightarrow$ $2p^3_{\frac{3}{2}} 5t^6_{2g}$ (intermediate state) $\rightarrow$ $2p^4_{\frac{3}{2}} 5t^5_{2g}$ (final state), where the final state can be the ground state itself or an excited state. When evaluating the matrix elements of Eq. 5.15, we neglect the radial part because this is common to all transitions and can therefore be integrated out. Having expressed the $5d$–t_{2g} states and the dipole operator in terms of spherical harmonics, it remains to write an expression for the intermediate $2p_{\frac{3}{2}}$ states which are split by spin-orbit coupling

$$|p_{\frac{3}{2},\frac{3}{2}}\rangle = |Y_1^1, \uparrow\rangle \tag{5.17a}$$

$$|p_{\frac{3}{2},\frac{1}{2}}\rangle = \sqrt{\frac{2}{3}} (|Y_1^0, \uparrow\rangle + \frac{1}{\sqrt{3}} (|Y_1^1, \downarrow\rangle) \tag{5.17b}$$

$$|p_{\frac{3}{2},-\frac{1}{2}}\rangle = \sqrt{\frac{2}{3}} (|Y_1^0, \downarrow\rangle + \frac{1}{\sqrt{3}} (|Y_1^{-1}, \uparrow\rangle) \tag{5.17c}$$

$$|p_{\frac{3}{2},-\frac{3}{2}}\rangle = |Y_1^{-1}, \downarrow\rangle\,. \tag{5.17d}$$

This way, the matrix elements in Eq. 5.15 reduce to the integral of three spherical harmonics and can be easily calculated. By means of basis change transformation, we can then rewrite matrix elements in terms of t_{2g} states. Note that we did not consider $2p_{\frac{1}{2}}$ states because spin-orbit coupling of Ir $2p$ state is huge ($\approx$ 1 keV) and interference terms between $2p_{\frac{1}{2}}$ and $2p_{\frac{3}{2}}$ intermediate states can safely be neglected.

Results are conveniently expressed in terms of a so-called atomic scattering tensor $\mathcal{A}_{|f,\pm\rangle}$, defined as

$$\mathcal{A}^{\boldsymbol{\epsilon}\boldsymbol{\epsilon}'}_{|f,\pm\rangle} \equiv \boldsymbol{\epsilon}'^{*}\, \mathcal{A}_{|f,\pm\rangle}\, \boldsymbol{\epsilon}. \tag{5.18}$$

$\mathcal{A}_{|f,\pm\rangle}$ contains physical parameters such as crystal field splitting and spin-orbit coupling. The dependence of scattering geometry and photons polarization is instead encoded in $\boldsymbol{\epsilon}$ and $\boldsymbol{\epsilon}'$. In the case of elastic scattering, where the initial and final state coincide with the ground state, say $|0,-\rangle$, the atomic scattering tensor reads

$$\mathcal{A}_{|0,-\rangle} = \begin{pmatrix} \frac{2(7+A+A^2)}{3(2+A^2)} & \frac{-i[10+(-2+A)A]}{3(2+A^2)} & 0 \\ \frac{i[10+(-2+A)A]}{3(2+A^2)} & \frac{2(7+A+A^2)}{3(2+A^2)} & 0 \\ 0 & 0 & \frac{2(1+2A^2)}{3(2+A^2)} \end{pmatrix}. \tag{5.19}$$

Similarly one can derive the atomic scattering tensor to all possible final states (reported in Appendix A). In our case, measurements were performed on powder sample, so in order to compare our calculations to experimental results, RIXS cross-sections should be averaged over all directions in space and the scattering angle should be fixed at 90°. For elastic scattering, the REXS ($|f,\pm\rangle = |0,-\rangle$) cross-section is

$$\sigma_{|0,-\rangle} = \frac{2(10+(A(A-2)))^2}{9(2+A^2)^2}, \tag{5.20}$$

e. g. the sum of the squares of the off-diagonal terms in Eq. 5.19.

5.5 Results and discussion

The energies of peaks A and B in the spectrum of Rb_2IrF_6 in Fig. 5.5 can be explained by considering the model Hamiltonian described above. By constraining the energies of the $|1,\pm\rangle$ and $|2,\pm\rangle$ states at 0.83 and 0.94 eV or vice versa, we obtain estimates for the effective trigonal crystal field splitting and spin-orbit coupling of $\Delta_{tri} = 0.183$ and $\zeta = 0.582$ eV or $\Delta_{tri} = -0.162$ and $\zeta = 0.585$ eV, respectively. The values of these two solutions are reported in Fig. 5.8 (pink and green dashed lines). Both values of ζ agrees with previous estimates [31, 32, 42, 45, 6, 68]. That the estimate of ζ does not change in the two cases is consistent with the fact that the value of the spin-orbit coupling is mostly dictated by the center of mass of the two peaks.

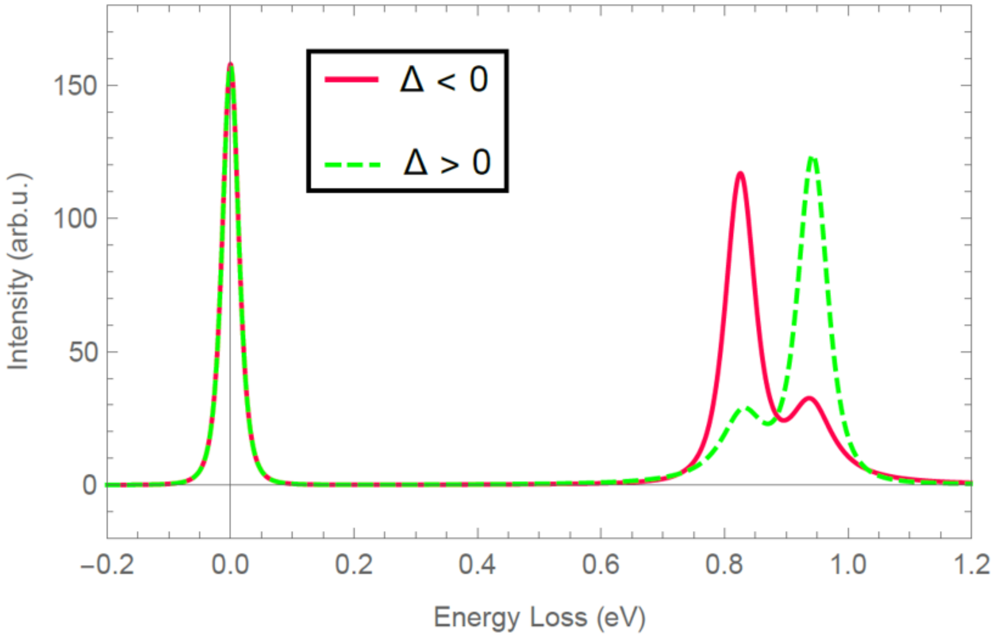

Figure 5.9: Simulated RIXS spectra of Rb_2IrF_6 in the case of $\Delta_{tri} > 0$ (green dashed line) and $\Delta_{tri} < 0$ (red continuous line).

At this stage, we invoke the calculations of the RIXS cross-sections to rule out one of the two solutions. Fig. 5.9 shows the calculated RIXS intensities in the two cases, $\Delta_{tri} < 0$ (red continuous) and $\Delta_{tri} > 0$ (green dashed line). The calculated RIXS spectrum is obtained by normalising each of the two fitting curves reproducing features A and B to the calculated spectral weight while keeping their energy, width and shape fixed to the fitted value. In the red curve of Fig. 5.9 the low energy peak is more intense than the high energy one, whereas it is the opposite for the green curve. It is therefore immediate to conclude that the red curve, *i.e.* the one obtained for $\Delta_{tri} = -0.163$ eV, better reproduces the experimental RIXS spectrum of Fig. 5.5. A negative value of the trigonal crystal field splitting suggests that the IrO_6 octahedron is compressed along the [1 1 1] axis, in agreement with crystallographic studies [69].

It should be noted, however, that knowledge of the sample crystallography alone could not be used to discard one solution: as an example, we mention the case of Ba_2IrO_4 [32] and Sr_2IrO_4 [23] where the sign of the tetragonal distortion is opposite despite the fact that the IrO_6 octahedra are elongated in the [0 0 1] direction in both samples.

The values of the crystal field splitting and spin-orbit coupling at 300 and 10 K for all the samples measured are reported in Tab. 5.2.

	300 K		**10 K**	
	Δ (eV)	ζ (eV)	Δ (eV)	ζ (eV)
$\boldsymbol{Li_2IrF_6}$ *	-0.16	0.58	-0.21	0.59
$\boldsymbol{Na_2IrF_6}$*	-0.16	0.59	-0.25	0.58
$\boldsymbol{K_2IrF_6}$	-0.16	0.58	-0.16	0.58
$\boldsymbol{Rb_2IrF_6}$	-0.16	0.58	-0.16	0.59
$\boldsymbol{Cs_2IrF_6}$	-0.15	0.58	-0.15	0.58
$\boldsymbol{SrIrF_6}$	-0.16	0.59	-	-
$\boldsymbol{BaIrF_6}$	-0.16	0.59	-0.14	0.59

Table 5.2: Effective trigonal/tetragonal crystal field splitting and spin-orbit coupling of the various compounds at 10 and 300 K. The symbol * indicates compounds which are characterized by a tetragonal distortion of the IrF_6 octahedron.

For convenience, these values are plotted in Fig. 5.10 where we can see that the spin-orbit coupling (right panel of Fig. 5.10) is practically temperature independent, as expected, while the effective crystal field splitting (left panel of Fig. 5.10) changes dramatically in samples with tetragonal distortion of the octahedral cage (Li_2IrF_6 and Na_2IrF_6) and marginally in the samples with trigonal distortion. A detailed temperature dependence of Δ_{tetra} in Na_2IrF_6 is reported in Fig. 5.7(a). The interpretation of these results is not obvious and currently we are considering two different scenarios. In the first one, we assume the material to be homogeneous and the temperature dependence of

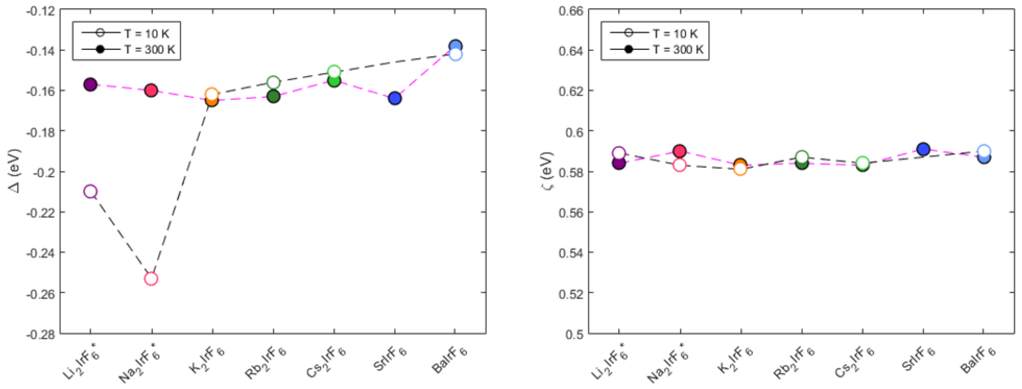

Figure 5.10: Effective trigonal/tetragonal crystal field splitting (left) and spin-orbit coupling (righ panel) of the various compounds at 10 (open circles) and 300 (filled circle) K. The symbol * indicates compounds which are characterized by a tetragonal distortion of the IrF_6 octahedron.

the RIXS spectra to be given by changes in the crystal structure. Within these assumptions, we decided to fit the RIXS spectra with one curve per peak and monitor their energy shift as a function of temperature. Values of the effective tetragonal crystal field splitting and spin-orbit coupling can be extracted in the temperature range 10 – 310 K, as summarised in Tab. 5.3. While ζ is almost temperature independent, as pointed out before, Fig. 5.11 shows that Δ_{tetra} varies considerably. To the best of our knowledge, no structural phase transition has been reported for Na_2IrF_6, so the temperature effect on the crystal field should be ascribed to the mere change in the lattice parameter.

Another scenario could be the one in which the material is inhomogeneous and two phases coexist at intermediate temperatures, characterised by different values of the crystal field, whose relative population changes with temperature. Indeed, the RIXS spectra at 235 K and neighbouring temperatures of Fig. 5.7(a) seem to suggest the presence of two components in feature A (and possibly two in feature B). We therefore decided to carry out an alternative type of analysis: we fitted the RIXS spectra of Na_2IrF_6 at 10 and 310 K, separately, and extracted the energies of features A and B ($x^A_{10K} = 0.805$ and $x^B_{10K} = 0.988$ eV at 10 K, $x^A_{310K} = 0.842$ and $x^B_{310K} = 0.953$ eV at 310 K);

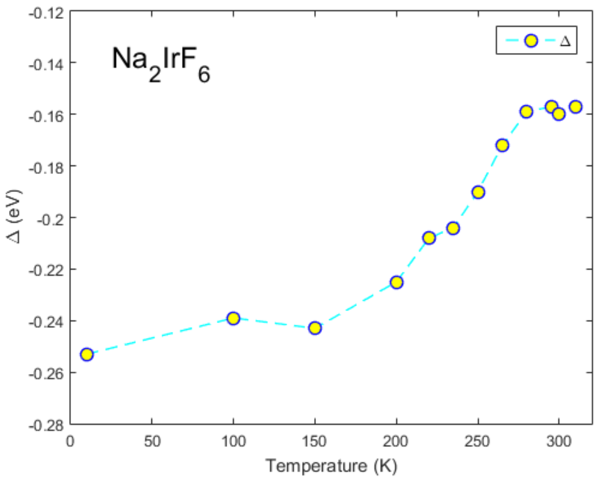

Figure 5.11: Effective tetragonal crystal field splitting of Na_2IrF_6 in the temperature range between 10 and 310 K. The numerical values are reported in Tab. 5.3.

	Δ (eV)	ζ (eV)
10 K	-0.25	0.58
100 K	-0.24	0.58
150 K	-0.24	0.58
200 K	-0.22	0.58
220 K	-0.21	0.59
235 K	-0.20	0.59
250 K	-0.19	0.59
265 K	-0.17	0.59
280 K	-0.16	0.59
295 K	-0.16	0.59
300 K	-0.16	0.59
310 K	-0.16	0.59

Table 5.3: Effective tetragonal crystal field splitting and spin-orbit coupling of Na_2IrF_6 in the temperature range between 10 and 310 K.

we then fitted all the remaining RIXS spectra with two curves per peak by constraining their energy positions to the values reported for 10 and 310 K, *e. g.* each spectrum has been fitted to four curves of fixed energy. As an example, we show in Fig. 5.12 the fitting to the spectrum of Na_2IrF_6 at 235 K. The idea is to explain the change in the peaks position with temperature as a shift of spectral weight between the two components. Fig. 5.13 shows the temperature evolution of the relative spectral weight of the two components, defined as $(w^A_{10K} - w^A_{310K})/(w^A_{10K} + w^A_{310K})$ and $(w^B_{10K} - w^B_{310K})/(w^B_{10K} + w^B_{310K})$, where w^A_{10K} is the spectral weight of the component centered at x^A_{10K}, and similarly for the other terms. The results are also reported in Tab. 5.4. According to this analysis, the two phases are almost identically distributed at around 235 K, for which $w^A_{10K} \simeq w^A_{310K}$ and $w^B_{10K} \simeq w^B_{310K}$. These two phases are characterised by effective tetragonal crystal field splitting and spin-orbit couplings given in Tab. 5.2 for 10 and 300 K, respectively.

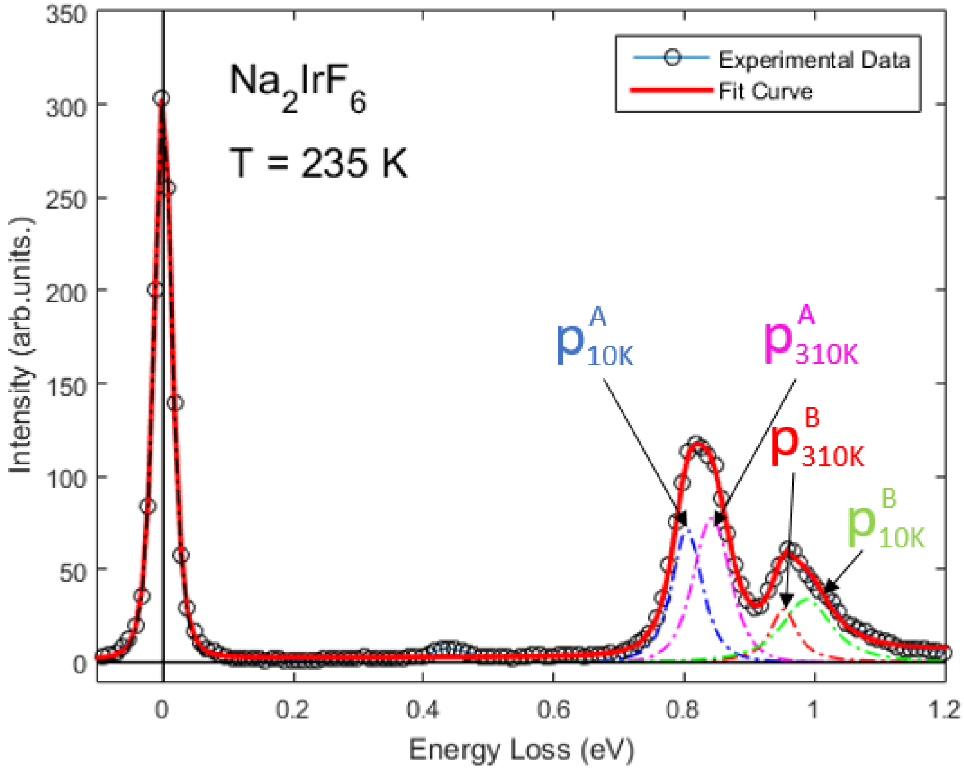

Figure 5.12: RIXS spectrum of Na_2IrF_6 at 235 K. Open circles represent the experimental data, the red line is the fit and the four different dashed lines are the fit to features A and B.

Currently, we can not distinguish between these two scenarios. For this reason, we are planning to perform high resolution powder diffraction measurements in order to:

i) check the presence of multiple phases in the material;

ii) track the evolution of the crystal structure down to the lowest temperature;

iii) better understand the distinct behaviour of materials with tetragonal and trigonal distortion of the IrF_6 octahedral cage.

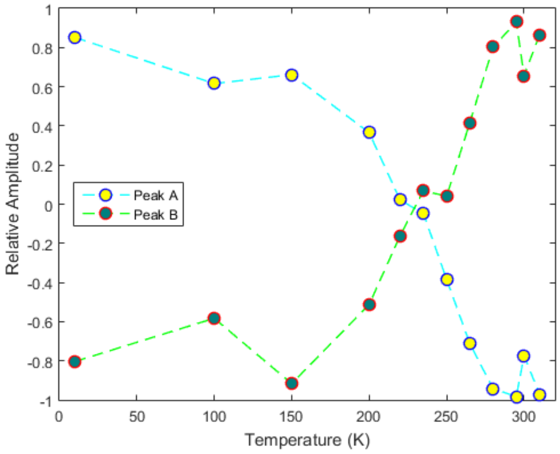

Figure 5.13: Evolution of the relative spectral weight of the two components in peak A (yellow circles) and B (green circles) for Na_2IrF_6 in the 10–310 K temperature range. The numerical values are reported in Tab. 5.4.

	Peak A	Peak B
10 K	0.85	-0.80
100 K	0.61	-0.58
150 K	0.66	-0.92
200 K	0.36	-0.51
220 K	0.21	-0.16
235 K	-0.05	0.07
250 K	-0.38	0.04
265 K	-0.71	0.42
280 K	-0.94	0.80
295 K	-0.98	0.93
300 K	-0.77	0.65
310 K	-0.97	0.86

Table 5.4: Evolution of the relative spectral weight of the two components of peaks A and B in Na_2IrF_6 in the 10–310 K temperature range.

5.6 Conclusions

Motivated by recent theoretical predictions about the possible realisation of a SU(2) symmetric ground state in Rb_2IrF_6[5], we performed RIXS measurements in a series of Ir fluorides, namely A_2IrF_6 (where A=Li, Na, K, Rb and Cs are the alkali metals) and $B IrF_6$ (where B=Sr and Ba are alkaline earth metals). We intepreted the results on the basis of a single ion model and assigned transitions to intra–t_{2g} excitations. We realised that two different solutions of the single ion Hamiltonian can equally well explain the splitting between features A and B, one with a positive and one with a negative value of the effective trigonal/tetragonal crystal field splitting of t_{2g} states. In order to make a distinction, we imposed a further constraint by calculating the RIXS cross-sections and concluded that the solution with negative Δ_{tri} better reproduces the experimental data.

In the specific case of Rb_2IrF_6, we determined that the distortion of the IrF_6 induces a splitting of the t_{2g} states consistent with an effective trigonal crystal field splitting $\Delta_{tri} = -0.16$ eV, *e. g.* a rather large value compared to model materials like Sr_2IrO_4 ($\Delta_{tetra} = -0.01$ eV [23]) or Ba_2IrO_4 ($\Delta_{tetra} = 0.05$ eV [32]). We therefore conclude that our measurements are not consistent with the calculations by Birol *et al.* [5], according to which the departure of Rb_2IrF_6 from the perfect cubic symmetry should be minimal. Nevertheless, RIXS spectra in Li_2IrF_6 and Na_2IrF_6 reveals that the effective crystal field splitting is extremely sensitive to temperature in Ir fluorides with tetragonal coordination of the IrF_6 octahedra. This suggests that the electronic structure of these compounds can easily be modified by acting on their crystal structure and calls for further future investigations.

Appendix A

RIXS atomic scattering tensors

A.1 Trigonal case

Here we report in detail the RIXS atomic scattering tensors and cross-sections for the Ir L_3-edge obtained in the single-ion model considering a trigonal distortion of the IrO_6 octahedron. The cross-sections will be averaged over all directions in space with a scattering angle fixed at 90°. In Chapter 5.4 we described how to get RIXS cross-sections in case of iridates, and in particular we have already shown the atomic scattering tensor for the elastic scattering (REXS, see Eq. 5.19), where the final state coincides with the initial one ($|f,\pm\rangle = |0,-\rangle$).

Of particular interest is the RIXS cross-section to the (pseudo)spin-flip state ($|f,\pm\rangle = |0,+\rangle$), relevant for magnetic excitations (also called magnons). In this case, the atomic scattering tensor and cross-section read

$$\mathcal{A}_{|0,+\rangle} = \begin{pmatrix} 0 & 0 & \frac{(2+A)(1+2A)}{3(2+A^2)} \\ 0 & 0 & \frac{-i(2+A)(1+2A)}{3(2+A^2)} \\ \frac{-(2+A)(1+2A)}{3(2+A^2)} & \frac{i(2+A)(1+2A)}{3(2+A^2)} & 0 \end{pmatrix}, \tag{A.1a}$$

$$\sigma_{|0,+\rangle} = \frac{4(2+A^2)(1+2A)^2}{9(2+A^2)^2}. \tag{A.1b}$$

Zero diagonal elements indicate that single magnon excitations must involve a rotation of the photon polarization, as in the case of Cu L_3-edge RIXS in cuprates [16].

The RIXS scattering atomic tensors and averaged cross-sections for the inelastic transitions are:

$$\mathcal{A}_{|1,-\rangle} = \begin{pmatrix} \frac{14+A-B-2AB}{3\sqrt{(2+A^2)(2+B^2)}} & \frac{i(-10A+(A-1)B)}{3\sqrt{(2+A^2)(2+B^2)}} & 0 \\ \frac{-i(-10A+(A-1)B)}{3\sqrt{(2+A^2)(2+B^2)}} & \frac{14+A-B-2AB}{3\sqrt{(2+A^2)(2+B^2)}} & 0 \\ 0 & 0 & \frac{-2(1+2A)(-1+2B)}{3\sqrt{(2+A^2)(2+B^2)}} \end{pmatrix}, \tag{A.2a}$$

$$\sigma_{|1,-\rangle} = \frac{2(-10+A+(A-1)B)^2}{9(2+A^2)^2(2+B^2)^2}, \tag{A.2b}$$

$$\mathcal{A}_{|1,+\rangle} = \begin{pmatrix} \frac{-3\sqrt{2}A-3\sqrt{2}B}{3\sqrt{(2+A^2)(2+B^2)}} & \frac{-3i\sqrt{2}A-3i\sqrt{2}B}{3\sqrt{(2+A^2)(2+B^2)}} & \frac{-(2+A)(-1+2B)}{3\sqrt{(2+A^2)(2+B^2)}} \\ \frac{-3i\sqrt{2}A-3i\sqrt{2}B}{3\sqrt{(2+A^2)(2+B^2)}} & \frac{+3\sqrt{2}A+3\sqrt{2}B}{3\sqrt{(2+A^2)(2+B^2)}} & \frac{i(2+A)(-1+2B)}{3\sqrt{(2+A^2)(2+B^2)}} \\ \frac{(1+2A)(-2+B)}{3\sqrt{(2+A^2)(2+B^2)}} & \frac{-i(1+2A)(-2+B)}{3\sqrt{(2+A^2)(2+B^2)}} & 0 \end{pmatrix}, \tag{A.3a}$$

$$\sigma_{|1,+\rangle} = \frac{2(8+5B(7B-4)+4A(5+5B+B^2)+A^2(35+4B(2B-5)))}{9(2+A^2)^2(2+B^2)^2}, \tag{A.3b}$$

$$\mathcal{A}_{|2,-\rangle} = \begin{pmatrix} \frac{-A-2}{3\sqrt{2(2+A^2)}} & \frac{i(A+2)}{3\sqrt{2(2+A^2)}} & \frac{2}{\sqrt{2+A^2}} \\ \frac{i(A+2)}{3\sqrt{2(2+A^2)}} & \frac{A+2}{3\sqrt{2(2+A^2)}} & \frac{2i}{\sqrt{2+A^2}} \\ \frac{2(1+2A)}{3\sqrt{2+A^2}} & \frac{2i(1+2A)}{3\sqrt{2+A^2}} & 0 \end{pmatrix}, \tag{A.4a}$$

$$\sigma_{|2,-\rangle} = \frac{11}{3} + \frac{2+4A}{2+A^2}, \tag{A.4b}$$

$$\mathcal{A}_{|2,+\rangle} = \begin{pmatrix} \frac{2+A}{3\sqrt{2+A^2}} & \frac{-i(2+A)}{3\sqrt{2+A^2}} & \frac{-A}{\sqrt{2(2+A^2)}} \\ \frac{-i(2+A)}{3\sqrt{2+A^2}} & \frac{-A-2}{3\sqrt{2+A^2}} & \frac{-iA}{\sqrt{2(2+A^2)}} \\ \frac{\sqrt{2}(1+2A)}{3\sqrt{2+A^2}} & \frac{i\sqrt{2}(1+2A)}{3\sqrt{2+A^2}} & 0 \end{pmatrix}, \tag{A.5a}$$

$$\sigma_{|2,+\rangle} = 3 + \frac{2(4A-7)}{3(2+A^2)}. \tag{A.5b}$$

A.2 Tetragonal case

Here we report the calculations of the RIXS cross-sections for L_3-edge in the case of tetragonal symmetry of the crystal field splitting. The most convenient basis set used to describe the t_{2g} states is d_{xy}, d_{yz} and d_{zx}, in which case the single ion Hamiltonian reads (in analogy to Eq. 5.6)

$$\mathcal{H} = \zeta \mathbf{L} \cdot \mathbf{S} + \frac{\Delta_{tetra}}{3} \left(2 \left|d_{xy}\right\rangle \left\langle d_{xy}\right| + \left|d_{yz}/d_{zx}\right\rangle \left\langle d_{yz}/d_{zx}\right|\right) \tag{A.6}$$

The corresponding eigenvalues are

$$E_0 = \frac{1}{4}\left(1 + \delta + \sqrt{\delta(\delta - 2) + 9}\right) \tag{A.7a}$$

$$E_1 = \frac{1}{4}\left(1 + \delta\sqrt{\delta(\delta - 2) + 9}\right) \tag{A.7b}$$

$$E_2 = -\frac{\zeta}{2}. \tag{A.7c}$$

where $\delta = \frac{2\Delta_{tetra}}{\zeta}$. Considering the tetragonal distortion instead of trigonal, the Kramers doublets become

$$|0, \pm\rangle = \frac{A \left|d_{xy}, \mp\right\rangle \mp \left|d_{yz}, \pm\right\rangle + i \left|d_{xz}, \pm\right\rangle}{\sqrt{2 + A^2}} \tag{A.8a}$$

$$|1, \pm\rangle = -\frac{B \left|d_{xy}, \mp\right\rangle \mp \left|d_{yz}, \pm\right\rangle + i \left|d_{xz}, \pm\right\rangle}{\sqrt{2 + B^2}} \tag{A.8b}$$

$$|2, \pm\rangle = \frac{\pm \left|d_{yz}, \pm\right\rangle + i \left|d_{xz}, \pm\right\rangle}{\sqrt{2}} \tag{A.8c}$$

where $A = \frac{-1+\delta+\sqrt{9+(\delta-2)\delta}}{2}$ and $B = \frac{-1+\delta-\sqrt{9+(\delta-2)\delta}}{2}$ take into account the effect of the tetragonal crystal field and SOC. The Kramers doublets are the eigenstates of the total Hamiltonian of the system, and in this case are directly dependent on the t_{2g} orbitals d_{xy}, d_{yz} and d_{xz}. Here we have considered the elongation along the crystallographic c axis in the $\mathrm{IrO_6}$ octahedra, and for this reason we did not change the basis as for trigonal case. As in the case discussed above, in the following we report the RIXS scattering atomic tensors and cross-sections averaged over all directions in space with a scattering angle fixed at 90°. For elastic scattering, the REXS scattering atomic tensors and cross-sections read

$$\mathcal{A}_{|0,-\rangle} = \begin{pmatrix} \frac{3A^2+(2+A)^2}{2(2+A^2)} & \frac{-3iA^2+i(2+A)^2}{2(2+A^2)} & 0 \\ \frac{3iA^2-i(2+A)^2}{2(2+A^2)} & \frac{3A^2+(2+A)^2}{2(2+A^2)} & 0 \\ 0 & 0 & \frac{6}{2+A^2} \end{pmatrix}, \tag{A.9a}$$

$$\sigma_{|0,-\rangle} = \frac{2(-2+(A(A-2)))^2}{(2+A^2)^2}. \tag{A.9b}$$

In case of (pseudo) spin flip we obtain

$$\mathcal{A}_{|0,+\rangle} = \begin{pmatrix} 0 & 0 & \frac{-3A}{2+A^2} \\ 0 & 0 & \frac{-i3A}{2+A^2} \\ \frac{3A}{2+A^2} & \frac{3iA}{2+A^2} & 0 \end{pmatrix}, \tag{A.10a}$$

$$\sigma_{|0,+\rangle} = \frac{36A^2}{(2+A^2)^2}. \tag{A.10b}$$

Finally, for the inelastic transitions

$$\mathcal{A}_{|1,-\rangle} = \begin{pmatrix} \frac{-(2+A)(B-2)-3AB}{2\sqrt{(2+A^2)(2+B^2)}} & \frac{-i(2+A)(B-2)+3iAB}{2\sqrt{(2+A^2)(2+B^2)}} & 0 \\ \frac{i(2+A)(B-2)-3iAB}{2\sqrt{(2+A^2)(2+B^2)}} & \frac{-(2+A)(B-2)-3AB}{2\sqrt{(2+A^2)(2+B^2)}} & 0 \\ 0 & 0 & \frac{6}{\sqrt{(2+A^2)(2+B^2)}} \end{pmatrix}, \tag{A.11a}$$

$$\sigma_{|1,-\rangle} = \frac{2(2+A+(A-1)B)^2}{(2+A^2)^2(2+B^2)^2}, \tag{A.11b}$$

$$\mathcal{A}_{|1,+\rangle} = \begin{pmatrix} 0 & 0 & \frac{-3A}{\sqrt{(2+A^2)(2+B^2)}} \\ 0 & 0 & \frac{-3iA}{\sqrt{(2+A^2)(2+B^2)}} \\ \frac{-3B}{\sqrt{(2+A^2)(2+B^2)}} & \frac{-3iB}{\sqrt{(2+A^2)(2+B^2)}} & 0 \end{pmatrix}, \tag{A.12a}$$

$$\sigma_{|1,+\rangle} = \frac{18(A^2+B^2)}{(2+A^2)(2+B^2)}, \tag{A.12b}$$

$$\mathcal{A}_{|2,-\rangle} = \begin{pmatrix} \frac{2+A}{\sqrt{2(2+A^2)}} & \frac{-i(2+A)}{\sqrt{2(2+A^2)}} & 0 \\ \frac{-i(2+A)}{\sqrt{2(2+A^2)}} & \frac{-2-A}{\sqrt{2(2+A^2)}} & 0 \\ 0 & 0 & 0 \end{pmatrix}, \tag{A.13a}$$

$$\sigma_{|2,-\rangle} = \frac{(2+A)^2)}{2+A^2}, \tag{A.13b}$$

$$\mathcal{A}_{|2,+\rangle} = \begin{pmatrix} 0 & 0 & \frac{2+A}{\sqrt{2(2+A^2)}} \\ 0 & 0 & \frac{-i(2+A)}{\sqrt{2(2+A^2)}} \\ 0 & 0 & 0 \end{pmatrix}, \tag{A.14a}$$

$$\sigma_{|2,+\rangle} = \frac{(2+A)^2)}{2+A^2}. \tag{A.14b}$$

Bibliography

[1] F. A. Wang and T. Senthil, Phys. Rev. Lett. **106**, 2 (2011).

[2] G. Cao, J. Bolivar, S. McCall, J. Crow, and R. Guertin, Phys. Rev. B **57**, R11039 (1998).

[3] B. J. Kim, H. Jin, S. J. Moon, J. Y. Kim, B. G. Park, C. S. Leem, J. Yu, T. W. Noh, C. Kim, S. J. Oh, J. H. Park, V. Durairaj, G. Cao, and E. Rotenberg, Phys. Rev. Lett. **101**, 1 (2008).

[4] B. J. Kim, H. Ohsumi, T. Komesu, S. Sakai, T. Morita, H. Takagi, and T. Arima, Science **323**, 1329 (2009).

[5] T. Birol and K. Haule, Phys. Rev. Lett. **114**, 2 (2015).

[6] H. Gretarsson, J. P. Clancy, X. Liu, J. P. Hill, E. Bozin, Y. Singh, S. Manni, P. Gegenwart, J. Kim, A. H. Said, D. Casa, T. Gog, M. H. Upton, H. S. Kim, J. Yu, V. M. Katukuri, L. Hozoi, J. Van Den Brink, and Y. J. Kim, Phys. Rev. Lett. **110**, 1 (2013).

[7] W. Witczak-Krempa, G. Chen, Y. B. Kim, and L. Balents, Annu. Rev. Condens. Matter Phys. **5**, 57 (2014).

[8] J. Bednorz and K. Muller, Zeitschrift für Phys. B Condens. Matter **64**, 189 (1986).

[9] C. Rial, E. Morán, M. A. Alario-Franco, U. Amador, and N. H. Andersen, Phys. C **278**, 122 (1997).

[10] M. K. Crawford, M. A. Subramanian, R. L. Harlow, J. A. Fernandez-Baca, Z. R. Wang, and D. C. Johnston, Phys. Rev. B **49**, 9198 (1994).

[11] D. Vaknin, S. K. Sinha, D. E. Moncton, D. C. Johnston, J. M. Newsam, C. R. Safinya, and H. E. King, Phys. Rev. Lett. **58**, 2802 (1987).

[12] S. Boseggia, R. Springell, H. C. Walker, A. T. Boothroyd, D. Prabhakaran, S. P. Collins, and D. F. McMorrow, J. Phys. Condens. Matter **24**, 312202 (2012).

[13] M. Imada, A. Fujimori, and Y. Tokura, Rev. Mod. Phys. **70**, 1039 (1998).

[14] R. Coldea, S. M. Hayden, G. Aeppli, T. G. Perring, C. D. Frost, T. E. Mason, S. W. Cheong, and Z. Fisk, Phys. Rev. Lett. **86**, 5377 (2001).

[15] L. Braicovich, J. Van Den Brink, V. Bisogni, M. M. Sala, L. J. P. Ament, N. B. Brookes, G. M. De Luca, M. Salluzzo, T. Schmitt, V. N. Strocov, and G. Ghiringhelli, Phys. Rev. Lett. **104**, 3 (2010).

[16] M. Moretti Sala, V. Bisogni, C. Aruta, G. Balestrino, H. Berger, N. B. Brookes, G. M. De Luca, D. Di Castro, M. Grioni, M. Guarise, P. G. Medaglia, F. Miletto Granozio, M. Minola, P. Perna, M. Radovic, M. Salluzzo, T. Schmitt, K. J. Zhou, L. Braicovich, and G. Ghiringhelli, New J. Phys. **13** (2011), 10.1088/1367-2630/13/4/043026.

[17] J. Kim, D. Casa, M. H. Upton, T. Gog, Y. J. Kim, J. F. Mitchell, M. Van Veenendaal, M. Daghofer, J. Van Den Brink, G. Khaliullin, and B. J. Kim, Phys. Rev. Lett. **108**, 1 (2012).

[18] J. Kim, M. Daghofer, a. H. Said, T. Gog, J. van den Brink, G. Khaliullin, and B. J. Kim, Nat. Commun. **5**, 4453 (2014).

[19] Y. K. Kim, O. Krupin, J. D. Denlinger, a. Bostwick, E. Rotenberg, Q. Zhao, J. F. Mitchell, J. W. Allen, and B. J. Kim, Science **345**, 187 (2014).

[20] Y. K. Kim, N. H. Sung, J. D. Denlinger, and B. J. Kim, Nat. Phys. , 1 (2015).

[21] Y. Yang, W.-S. Wang, J.-G. Liu, H. Chen, J.-H. Dai, and Q.-H. Wang, Phys. Rev. B **89**, 094518 (2014).

[22] Y. J. Yan, M. Q. Ren, H. C. Xu, B. P. Xie, R. Tao, H. Y. Choi, N. Lee, T. Zhang, and D. L. Feng, ArXiv **2**, 1506.06557 (2015).

[23] S. Boseggia, H. C. Walker, J. Vale, R. Springell, Z. Feng, R. S. Perry, M. Moretti Sala, H. M. Rønnow, S. P. Collins, and D. F. McMorrow, J. Phys. Condens. Matter **25**, 422202 (2013).

[24] H. Das and T. Saha-Dasgupta, Phys. Rev. B **79**, 134522 (2009).

[25] G. Kotliar and D. Vollhardt, Phys. Today **57**, 53 (2004).

[26] J. Hubbard, Proc. R. Soc. A Math. Phys. Eng. Sci. **276**, 238 (1963).

[27] Q. Li, G. Cao, S. Okamoto, J. Yi, W. Lin, B. C. Sales, J. Yan, R. Arita, J. Kuneš, A. V. Kozhevnikov, A. G. Eguiluz, M. Imada, Z. Gai, M. Pan, and D. G. Mandrus, Sci. Rep. **3**, 3073 (2013).

[28] S. Blundell, *"Magnetism in Condensed Matter"* (2001).

[29] S. J. Moon, M. W. Kim, K. W. Kim, Y. S. Lee, J.-Y. Kim, J.-H. Park, B. J. Kim, S.-J. Oh, S. Nakatsuji, Y. Maeno, I. Nagai, S. I. Ikeda, G. Cao, and T. W. Noh, Phys. Rev. B **74**, 113104 (2006).

[30] M. Moretti Sala, S. Boseggia, D. F. McMorrow, and G. Monaco, Phys. Rev. Lett. **112**, 1 (2014).

[31] M. M. Sala, K. Ohgushi, A. Al-Zein, Y. Hirata, G. Monaco, and M. Krisch, Phys. Rev. Lett. **112**, 176402 (2014).

[32] M. M. Sala, M. Rossi, S. Boseggia, J. Akimitsu, N. B. Brookes, M. Isobe, M. Minola, H. Okabe, H. M. Rønnow, L. Simonelli, and D. F. Mcmorrow, **121101**, 1 (2014).

[33] E. Francisco, **55**, 1355 (1985).

[34] L. Mattheiss, Phys. Rev. B **13**, 2433 (1976).

[35] B. B. A. Abragam, *"Electron Paramagnetic Resonance of Transitions Ions"* (1970).

[36] H. Meskine, Z. S. Popović, and S. Satpathy, Phys. Rev. B **65**, 094402 (2002).

[37] H. Okabe, M. Isobe, E. Takayama-Muromachi, A. Koda, S. Takeshita, M. Hiraishi, M. Miyazaki, R. Kadono, Y. Miyake, and J. Akimitsu, Phys. Rev. B - Condens. Matter Mater. Phys. **83**, 1 (2011).

[38] K. Matsuhira, M. Wakeshima, Y. Hinatsu, and S. Takagi, J. Phys. Soc. Japan **80**, 094701 (2011).

[39] R. Comin, G. Levy, B. Ludbrook, Z. H. Zhu, C. N. Veenstra, J. A. Rosen, Y. Singh, P. Gegenwart, D. Stricker, J. N. Hancock, D. Van Der Marel, I. S. Elfimov, and A. Damascelli, Phys. Rev. Lett. **109**, 1 (2012).

[40] J. G. Cheng, J. S. Zhou, J. B. Goodenough, Y. Sui, Y. Ren, and M. R. Suchomel, Phys. Rev. B - Condens. Matter Mater. Phys. **83**, 1 (2011).

[41] J. W. Kim, Y. Choi, J. Kim, J. F. Mitchell, G. Jackeli, M. Daghofer, J. Van Den Brink, G. Khaliullin, and B. J. Kim, Phys. Rev. Lett. **109**, 1 (2012).

[42] X. Liu, V. M. Katukuri, L. Hozoi, W. G. Yin, M. P. M. Dean, M. H. Upton, J. Kim, D. Casa, A. Said, T. Gog, T. F. Qi, G. Cao, A. M. Tsvelik, J. Van Den Brink, and J. P. Hill, Phys. Rev. Lett. **109**, 2 (2012).

[43] H. Gretarsson, J. P. Clancy, Y. Singh, P. Gegenwart, J. P. Hill, J. Kim, M. H. Upton, A. H. Said, D. Casa, T. Gog, and Y. J. Kim, Phys. Rev. B - Condens. Matter Mater. Phys. **87**, 1 (2013).

[44] L. Hozoi, H. Gretarsson, J. Clancy, B.-G. Jeon, B. Lee, K. Kim, V. Yushankhai, P. Fulde, Y.-J. Kim, and J. van den Brink, ArXiv e-prints , 5 (2012).

[45] E. Lefrançois, a. M. Pradipto, M. M. Sala, L. C. Chapon, V. Simonet, S. Picozzi, P. Lejay, and R. Ballou, , 2 (2015), arXiv:1504.05420 .

[46] L. J. P. Ament, M. Van Veenendaal, T. P. Devereaux, J. P. Hill, and J. Van Den Brink, Rev. Mod. Phys. **83**, 705 (2011), arXiv:1009.3630 .

[47] L. J. P. Ament, G. Ghiringhelli, M. M. Sala, L. Braicovich, and J. Van Den Brink, Phys. Rev. Lett. **103**, 9 (2009).

[48] P. Glatzel, M. Sikora, and M. Fernández-García, Eur. Phys. J. Spec. Top. **169**, 207 (2009).

[49] L. J. P. Ament, G. Khaliullin, and J. Van Den Brink, Phys. Rev. B - Condens. Matter Mater. Phys. **84**, 2 (2011).

[50] S. G. Chiuz??ian, G. Ghiringhelli, C. Dallera, M. Grioni, P. Amann, X. Wang, L. Braicovich, and L. Patthey, Phys. Rev. Lett. **95**, 3 (2005).

[51] G. Ghiringhelli, N. B. Brookes, E. Annese, H. Berger, C. Dallera, M. Grioni, L. Perfetti, A. Tagliaferri, and L. Braicovich, Phys. Rev. Lett. **92**, 117406 (2004).

[52] M. Matsubara, T. Uozumi, A. Kotani, Y. Harada, and S. Shin, J. Phys. Soc. Japan **69**, 1558 (2000).

[53] A. Kotani and S. Shin, Rev. Mod. Phys. **73**, 203 (2001).

[54] J. Cullie J. Sparks, Phys. Rev. Lett. **33**, 262 (1974).

[55] J. P. Hill, G. Blumberg, Y. J. Kim, D. S. Ellis, S. Wakimoto, R. J. Birgeneau, S. Komiya, Y. Ando, B. Liang, R. L. Greene, D. Casa, and T. Gog, Phys. Rev. Lett. **100**, 3 (2008).

[56] M. Minola, *"Magnetic, Orbital and Charge Fluctuations in Layered Cuprates Studied By Resonant Soft X-Ray Scattering"*, (2013).

[57] M. Blume, J. Appl. Phys. **57**, 3615 (1985).

[58] S. Boseggia, *"Magnetic order and excitations in perovskite iridates studied with resonant X-ray scattering techniques"* (2014).

[59] J. K. D. Vaughan, *"X-Ray Data Booklet"* (2009).

[60] ESRF, "What is a synchrotron?" .

[61] M. Rossi, *"X-ray Raman Spectroscopy on Iridate Perovskites"* (2014).

[62] N. W. M. Ashcroft, *"Solid State Physics"* (1976).

[63] W. Massa and D. Babel, Chem. Rev. **88**, 275 (1988).

[64] D. Babel, *"Structural Chemistry of Octahedral Fluorocomplexes of the Transitions Elements"*, edited by B. Springer (1967).

[65] E. M. Plotnikova, M. Daghofer, J. van den Brink, and K. Wohlfeld, **106401**, 1 (2016), arXiv:1601.07069 .

[66] C. Ballhausen, *"Introduction to Ligand Field Theory"*, edited by McGraw-Hill (1962).

[67] D. J. Griffiths, *"Introduction to Quantum Mechanics"* (1995).

[68] S. Boseggia, R. Springell, H. C. Walker, H. M. Rønnow, C. Rüegg, H. Okabe, M. Isobe, R. S. Perry, S. P. Collins, and D. F. Mcmorrow, Phys. Rev. Lett. **110**, 1 (2013).

[69] A. I. Smolentsev, A. I. Gubanov, D. Y. Naumov, and A. M. Danilenko, Acta Crystallogr. Sect. E Struct. Reports Online **63**, i200 (2007).

Acknowledgments

The research included in this dissertation could not have been performed if not for the assistance, patience, and support of many people.

First of all, I would like to extend my gratitude to Prof. Giacomo Ghiringhelli for the great opportunity he gave me to stay at the ESRF and for trusting me.

Special thanks go to my supervisor at the ESRF, Dott. Marco Moretti (sometimes Sala), who kindly hosted me at ID20 beamline. Thanks for all the time he devoted to me and for encouraging me everyday to do my best, I really appreciated your continuous support during my traineeships at ID20.

Very special thanks go to Matteo, not only a colleague, but also a brother for me. We shared unforgettable moments, from interminable beamtime spent side by side trying to put the sample in the anvil cell to glorious weekends riding bike along the mountains of the Tour de France. Thanks for the continuous help and for all valuable advices.

I would like to thank all staff of ID20 beamline. Thanks to Christoph and Chiara for endless coffee and nice discussions after every delicious lunch at the canteen, and thanks to Christian, the “ID20 cornerstone”.

Thanks to all people I met at the ESRF and in Grenoble, in particular the other trainees from Politecnico: I can not forget every moment spent with you.

Special thanks go to my friends of a life, Rasco, Andre, Bobo, Turo, Ale,

Figure A.1: ID20 beamline staff. From the left: Marco Moretti, Christian Henriquet, Christoph Sahle, Myself, Chiara Cavallari and Matteo Rossi.

Teo, Otto and Ste, always available and always ready to give me a smile, specially in difficult moments. Thanks to Facco and his wife Chiara, because without them I could not discover the fantastic world of Engineering Physics.

Thanks to my travel companions in this long six years for every discussion, from football to physics and, off course, for lesson notes.

Thanks to my next–door neighbours, for hosting me every Sunday for football matches and for nice cakes.

I would like to extend my deepest gratitude to my parents, without whose love, support and understanding I would never have completed this master degree. Thanks to my sister and Gaetano, parents of the most beautiful children of the world. Thanks to the rest of my family, from uncles and aunts to my cousins, always by my side.

Finally, thanks to Annalisa, who is so precious for me. We spent all these

years together, facing each moment with the awareness of not being alone. We passed wonderful and difficult moments, sometimes we believed it was impossible to get here, and now it is time to look back and be proud of what we did. Thanks for everything.